

FLG

DNA 3864T

AD A 022850

SIMULATION OF FLUID MOTION IN CONTAINERS EXPOSED TO BLAST AND SHOCK ENVIRONMENTS

12

R&D Associates
P. O. Box 9695
Marina del Rey, California 90291

February 1975

Topical Report

CONTRACT No. DNA J01-74-C-0139

APPROVED FOR PUBLIC RELEASE;
DISTRIBUTION UNLIMITED.

THIS WORK SPONSORED BY THE DEFENSE NUCLEAR AGENCY
UNDER SUBTASK P99QAXDB001-13.

Prepared for
Director
DEFENSE NUCLEAR AGENCY
Washington, D. C. 20305

DDDC
RECEIVED
APR 7 1976
REGULATED
D



Destroy this report when it is no longer
needed. Do not return to sender.

UNCLASSIFIED

SECURITY CLASSIFICATION OF THIS PAGE (When Data Entered)

19 REPORT DOCUMENTATION PAGE		READ INSTRUCTIONS BEFORE COMPLETING FORM	
18 DNA 8864T	2. GOVT ACCESSION NO.	3. RECIPIENT'S CATALOG NUMBER	9
6 SIMULATION OF FLUID MOTION IN CONTAINERS EXPOSED TO BLAST AND SHOCK ENVIRONMENTS.		7. REPORT PERIOD COVERED Topical Report	
10 E. J. Chapyak H. F. Cooper		8. PERFORMING ORG. REPORT NUMBER RDA-TR-5900-001	
9. PERFORMING ORGANIZATION NAME AND ADDRESS R & D Associates P. O. Box 9695 Marina del Rey, California 90291		14. CONTRACT OR GRANT NUMBER(s)	
11. CONTROLLING OFFICE NAME AND ADDRESS Director Defense Nuclear Agency Washington, D.C. 20305		15. DNA 801-74-C-8139	
16 DNA-NWED-QAXD		10. PROGRAM ELEMENT, PROJECT, TASK AREA & WORK UNIT NUMBERS Subtask P99QAXDB001-13	
17 B001		11. Feb 1975	
12. DISTRIBUTION STATEMENT (of this Report) Approved for public release; distribution unlimited.		12. 58p	
13. DISTRIBUTION STATEMENT (of the abstract entered in Block 20, if different from Report)		15. SECURITY CLASS (of this Report) UNCLASSIFIED	
18. SUPPLEMENTARY NOTES This work sponsored by the Defense Nuclear Agency under Subtask P99QAXDB001-13.		15a. DECLASSIFICATION/DOWNGRADING SCHEDULE	
19. KEY WORDS (Continue on reverse side if necessary and identify by block number)			
Blast Shock Simulation Fluid Motion		Pools Canals Nuclear Weapons Effects MIXED COMPANY III	
20. ABSTRACT (Continue on reverse side if necessary and identify by block number) The problem of simulating fluid motion in open containers that are subjected to the effects of nuclear weapons is examined in detail. Results obtained from experiments included on the MIXED COMPANY III high explosive test and laboratory shake-table tests are analyzed with the aid of supporting theoretical analysis. A fluid loss prediction technique is developed and applied to configurations of interest.			

DD FORM 1 JAN 73 1473

EDITION OF 1 NOV 65 IS OBSOLETE

UNCLASSIFIED

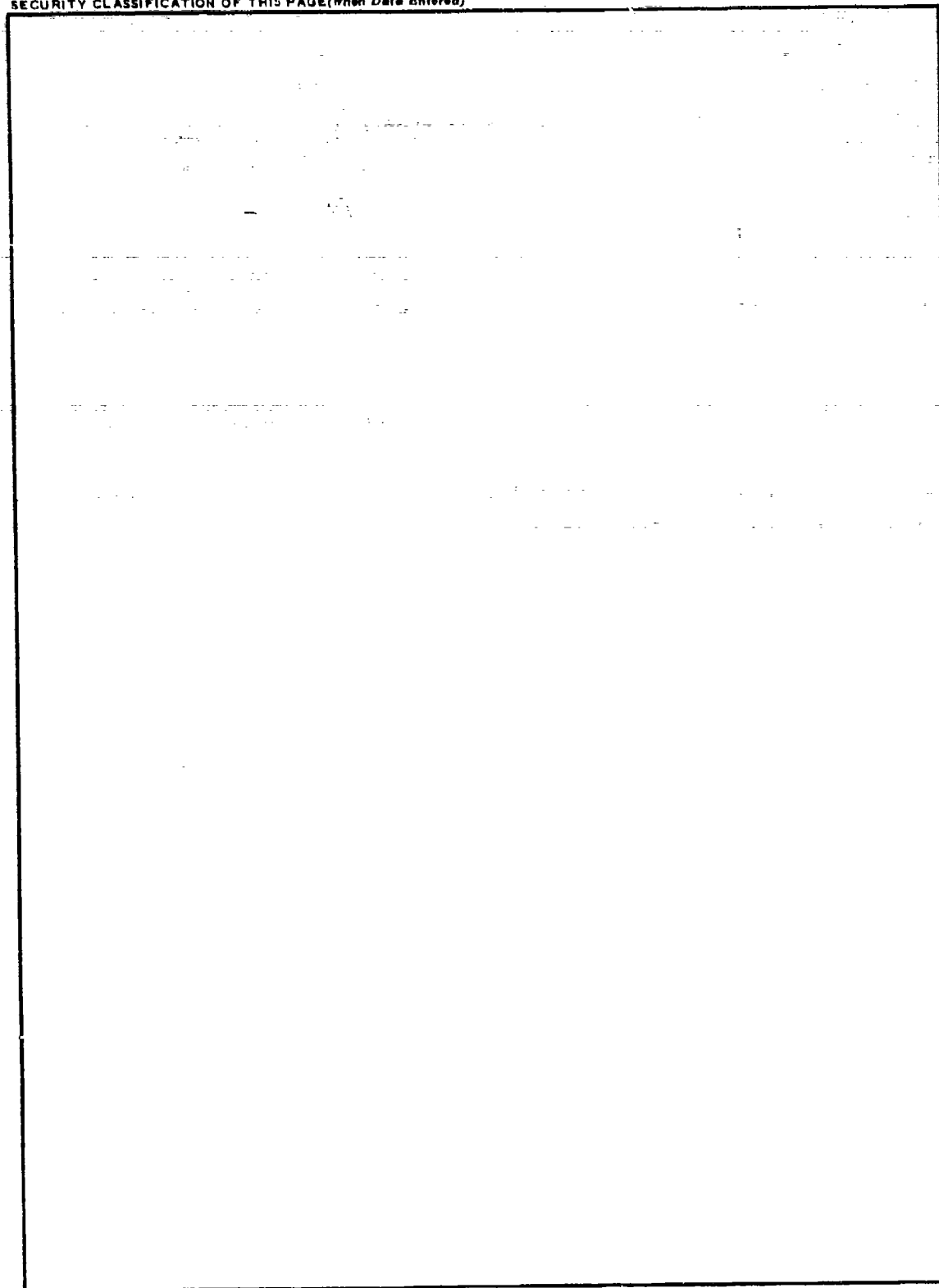
SECURITY CLASSIFICATION OF THIS PAGE (When Data Entered)

390124

JB

UNCLASSIFIED

SECURITY CLASSIFICATION OF THIS PAGE(When Data Entered)



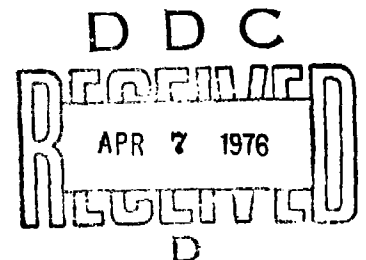
UNCLASSIFIED

SECURITY CLASSIFICATION OF THIS PAGE(When Data Entered)

SUMMARY

Water losses from canals, pools, etc., exposed to the effects of nearby nuclear explosions are caused by ground motions, airblast loading, and impacting debris. Certain of these phenomena are reasonably well understood and can be modeled with confidence, e.g., fluid motion induced by ground motion and overpressure loading. Other phenomena that could contribute to fluid loss are less well understood and can be modeled only with poor confidence, e.g., the growth of surface instabilities under dynamic pressure loading. Impacting debris is representative of a third class of loss mechanisms in that the water loss could conceivably be prescribed as a function of impact velocity, mass and shape of debris, etc.; yet still be poorly characterized because of the uncertainties in specifying the debris environment. This report omits any analysis of water loss produced by impacting debris (although debris certainly contributed to the fluid loss observed on high-explosive cratering experiments). Rather, we concentrate on fluid motion induced by ground motion and overpressure loading--and provide some comment on fluid response associated with complex interactions between the airblast dynamic pressure and the fluid's free surface.

Our approach is to assume the existence of a causal relationship between the maximum wave response and the water loss, and to obtain data to quantify this relationship. Analytic solutions for fluid response (in rectangular containers) to ground motion excitation are obtained and compared to data from controlled laboratory shake-table experiments. We find that, for horizontal, sinusoidal ground motion loading conditions of frequency f , the depth removed (Δd) is proportional to the amplitude of the displacement input (a), i.e., $\Delta d = \lambda(f) \cdot a$ where $\lambda(f)$ is a frequency-dependent constant of proportionality. The theoretically determined maximum wave response (h) is also proportional to the amplitude of the input displacement amplitude; i.e., $h = \gamma(f) \cdot a$ where $\gamma(f)$ is a frequency-dependent constant of proportionality. Furthermore, it appears



that $\gamma(f) \approx \Gamma \lambda(f)$ where Γ is a constant for all rectangular geometries examined. Based on this observation, we hypothesize that the fractional depth loss is given by

$$\frac{\Delta d}{d} = \Gamma \frac{h}{d},$$

where Γ is a constant for a given container geometry ($\Gamma \approx 0.31$ for rectangular containers) and d is the container depth. The above hypothesis is used to estimate fluid loss from containers exposed to combined airblast-horizontal ground motion environments. Such predictions are consistent with data obtained from MIXED COMPANY, although the estimates lie on the low side of the data scatter. This disagreement may be due to the effects of dynamic pressure, vertical ground motion, and impacting debris, which are ignored in the wave height calculation.

Following the encouraging comparison with MIXED COMPANY data, we estimate fluid losses from typical large-scale containers subjected to airblast and ground motions predicted for nuclear explosions. This analysis suggests that the relative portion of fluid loss associated with ground motion varies considerably with yield, container dimension and geologic variations of interest.[†] In some cases, airblast loading dominates. For example, when large trenches (≈ 300 -ft length) in dry soil are subjected to low-yield surface bursts, airblast effects dominate the close-in fluid loss, while ground motion effects dominate the close-in fluid loss for trenches exposed to large yields in wet soil. The worst case is associated with wet geologies

These results may underestimate the actual fluid loss because contributions associated with dynamic pressure and debris impact have not been considered. Additional studies are required to assess the water loss likely to be connected with such effects. However, it is believed that only minor perturbations to the fluid loss predictions presented here will be introduced by these phenomena.

[†]Airblast-induced water loss is independent of geology except in a second order sense which considers coupled airblast and ground motion effects.

Water loss from trenches, canals, pools, etc., may be prevented or significantly reduced with the use of berms placed around their perimeters. As a practical matter, the cost of berms would be nominal because excavated soil would be readily available for their construction. The waveheight calculations discussed in this paper could be used to develop design criteria for berm features (e.g., berm height) once the threat environment and soil geology are specified.

ACCESSION for		
NTIS	White Section	<input checked="" type="checkbox"/>
DOC	Dark Section	<input type="checkbox"/>
UNANNOUNCED		<input type="checkbox"/>
JUSTIFICATION.....		
BY.....		
DISTRIBUTION/AVAILABILITY CODES		
Dist.	AVAIL. and/or	SPECIAL
A		

TABLE OF CONTENTS

	<u>Page</u>
Summary	1
1. Introduction	7
2. Governing Equations and Scaling for Ground Motion and Overpressure Effects	10
2.1 Scaling Requirements	10
2.2 Overpressure Impulse Scaling	13
2.3 Quarter Root of Yield Scaling	14
2.4 Ground Motion Scaling	14
3. Dynamics of Fluid Response to Ground Motion and Overpressure	16
3.1 Formulation	16
3.2 Fast Decay Approximation	20
3.3 Step Wave Approximation	20
4. Dynamic Pressure and Vertical Ground Motion Effects	22
4.1 Kelvin-Helmholtz (K-H) Wave Generation	22
4.2 Approximate Treatment of Kelvin- Helmholtz Wave Generation and Vertical Ground Motion	23
4.3 Application to the Kelvin-Helmholtz Mechanism	25
4.4 Application to Vertical Ground Motion	27
4.5 Summary	28
5. Field Test and Laboratory Ground Shock Simulation Experiments	29
5.1 Introduction	29
5.2 Interpretation of Laboratory Experiments	31
5.3 Comparison with Field Test Data	35
6. Prediction of Fluid Loss in a Nuclear Environment	43
6.1 Characterization of the Environment	43
6.2 Prediction Calculations	44

TABLE OF CONTENTS (continued)

7. Conclusions and Summary	
7.1 Scaling Requirements	50
7.2 Analytical Results	50
7.3 Experimental Results	51
7.4 Recommendations	51
References	53

LIST OF FIGURES

<u>Figure</u>	<u>Title</u>	<u>Page</u>
1.1	Blast and Shock-Induced Fluid Motion in a Rectangular Trench	8
5.1	MIXED COMPANY Container	30
5.2	Maximum Wave Height Form Factor as a Function of Nondimensional Displacement Waveform Frequency . . .	33
5.3	Fractional Depth Loss Measurement as a Function of Normalized Maximum Wave Height	34
5.4	Fractional Depth Loss Measurement as a Function of Normalized Maximum Wave Height ($f_0/f < 1$)	36
5.5	Fractional Depth Loss Predictions and Experimental Results as a Function of Nondimensional Frequency for Various Values of Nondimensional Input Displacement Amplitude	37
5.6	Fractional Depth Loss Predictions and Experimental Results as a Function of Nondimensional Frequency for Various Values of Nondimensional Input Displacement Amplitude	38
5.7	Peak Surface (1.5-ft depth) Horizontal Displacement on MIXED COMPANY	40
5.8	MIXED COMPANY Data and Predictions (neglecting Vertical Ground Motion, Debris Impact and Dynamic Pressure Effects) for Small Containers	42
6.1	Predicted Depth Loss as a Function of Peak Overpressure and Yield for Dry Geologic Conditions . . .	45
6.2	Predicted Depth Loss as a Function of Peak Overpressure and Yield for Dry Geologic Conditions . . .	46
6.3	Predicted Depth Loss as a Function of Peak Overpressure and Yield for Wet Geologic Conditions . . .	47
6.4	Predicted Depth Loss as a Function of Peak Overpressure and Yield for Wet Geologic Conditions . . .	48

SECTION 1

INTRODUCTION

The effects of nuclear bursts on water-filled canals, pools, etc., are of interest for a variety of reasons [1]. The analysis presented here is concerned with airblast and ground shock induced fluid motion in a rectangular trench, where the blast wave is normal to the trench sidewalls (see Figure 1.1). We emphasize, however, that the choice of this particularly simple geometry is motivated only by our desire to simplify notation. Most of the results obtained here can be easily generalized to more complicated situations--both in the sense of container geometry and in the sense of blast wave direction relative to the container orientation. In any case, the geometry illustrated in Figure 1.1 is an excellent approximation to nearly all the field and laboratory experiments discussed in Section 5. Since the information obtained from these experiments consists almost entirely of post-shock fluid loss measurements, the theoretical effort presented here is directed primarily toward the development of a suitable fluid-loss prediction technique, although information on other important fluid response characteristics (e.g., the velocity field) is also obtained.

In principle, a complete description of fluid response in containers exposed to blast and shock effects from nuclear explosions can be derived from the governing equations for the appropriate boundary-initial value problem. Because ground displacement waveforms are mainly composed of low frequency components, which are essentially unaffected by the presence of shallow-buried structures, the free-field ground motions can be used as a displacement boundary condition for the pool side walls. In addition, the effect of airblast overpressure can be accurately represented as a pressure boundary condition for the fluid's free surface. However, although the ground motion and overpressure boundary conditions can be specified precisely, interactions between the airflow (dynamic pressure) and the free surface are not well understood and can only be approximately modeled. This fact, along with our suspicion that the water loss caused

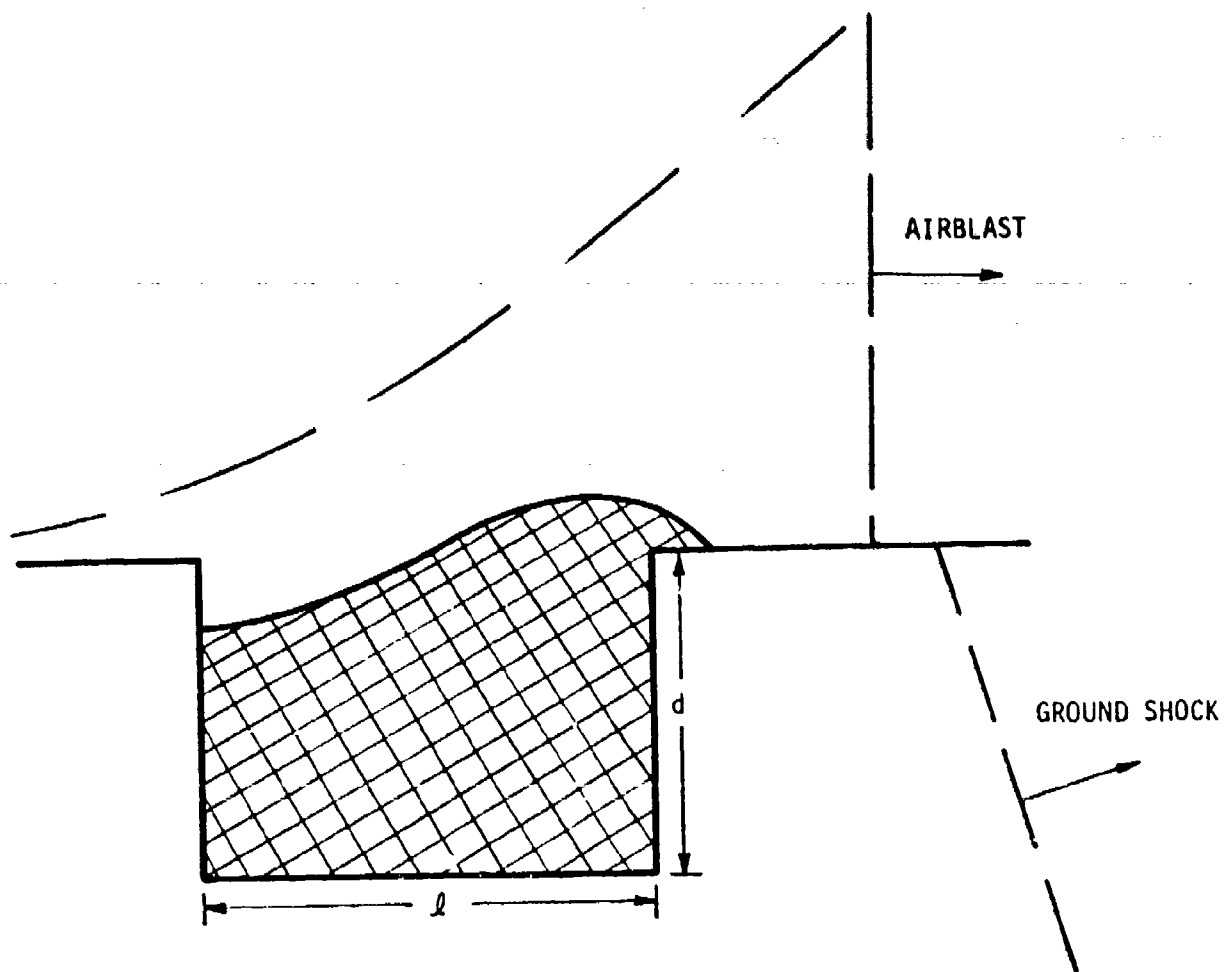


Figure 1.1 Blast and Shock-Induced Fluid Motion
in a Rectangular Trench

by dynamic pressure related forces may be of minor importance for the larger length scales of interest, lead us to first consider the effect of ground motion and overpressure on fluid response in Section 2, where a discussion of the complete boundary-initial value problem leads to scaling rules employed to design HE field experiments; and in Section 3, where a detailed, linearized analysis of fluid motion is presented. An examination of dynamic pressure effects, including scaling requirements, is presented in Section 4, while in Section 5, we consider the available experimental data in formulating a fluid loss prediction technique. Finally, Section 6 provides estimates of fluid loss in large-scale containers subjected to airblast and horizontal ground motion loading.

The water loss induced by impacting debris can also be modeled theoretically provided the debris size, shape and impact velocities are known. We shall not attempt to treat the effect of debris impact here. Other studies, beyond the scope of this paper, will consider possible bounds to water loss associated with impacting debris (as well as the potential hazards of impacting missiles on the survivability of the contents of liquid shelters).

SECTION 2

GOVERNING EQUATIONS AND SCALING FOR GROUND MOTION AND OVERPRESSURE EFFECTS

2.1 Scaling Requirements

An examination of the governing equations for fluid response in open containers indicates that at least five separate scaling requirements must be satisfied to guarantee dynamic similarity of the fluid motion. In a practical sense, these requirements, which are associated with gravitational, viscous, surface tension, cavitation and compressible effects, cannot be simultaneously incorporated into the design of model experiments. It appears, however, that elimination of the non-gravitational scaling requirements may not seriously affect the properties of fluid motion which are important to blast and shock-induced fluid loss. In particular, viscosity and surface tension probably have a very minor effect on parameters such as maximum waveheight and net fluid loss, provided container dimensions are greater than a few inches. Likewise, cavitation (which may not even occur) and fluid compressibility are only important during passage of a strong air shock (>100 psi) over the fluid's surface. Air shock related compressive effects are currently being investigated; however, for the purposes of this report we shall assume that they do not seriously affect the fluid response characteristics mentioned above.

Consider an open, two-dimensional, rectangular fluid-container system[†] of length l and mean fluid depth d . Assume that the free surface of the fluid is subjected to an overpressure loading $P(x,t)$ and that the container undergoes a rigid body displacement, defined by the motion of surrounding ground material, $\vec{D}(t)$. By neglecting the fluid's

[†]The specialization to two-dimensional, rectangular containers is made only to simplify the notation. Generalization of the following procedure to a three-dimensional system of arbitrary geometry is straightforward. The results are unchanged.

viscosity, surface tension, and compressibility, and by introducing the length scale ℓ and time scale $\sqrt{\ell/g}$, the equations of motion and boundary conditions can be expressed in the non-dimensional form[†]

$$\nabla_{*}^2 \phi^{*} = 0 \text{ (Continuity equation),} \quad (2.1)$$

$$\left. \frac{\partial \eta}{\partial \tau} + \vec{\nabla}_{*} \eta^{*} \cdot \vec{\nabla}_{*} \phi^{*} \right|_{z^{*} = \eta^{*}} = \left. \frac{\partial \phi^{*}}{\partial z^{*}} \right|_{z^{*} = \eta^{*}}, \quad (2.2)^{++}$$

$$\left. \frac{\partial \phi^{*}}{\partial \tau} + \frac{\vec{\nabla}_{*} \phi^{*} \cdot \vec{\nabla}_{*} \phi^{*}}{2} \right|_{z^{*} = \eta^{*}} + \frac{P(x, t)}{\rho g \ell} + \eta^{*} = 0, \quad (2.3)^{++}$$

$$\left. \frac{\partial \phi^{*}}{\partial x^{*}} \right|_{x^{*} = \vec{D}(t) \cdot \vec{i} / \ell} = \left. \frac{\partial \phi^{*}}{\partial x^{*}} \right|_{x^{*} = 1 + \vec{D}(t) \cdot \vec{i} / \ell} \left. \begin{aligned} &= \frac{1}{\ell} \frac{d\vec{D}(t)}{d\tau} \cdot \vec{i} \\ &= \frac{1}{\ell} \frac{d\vec{D}(t)}{d\tau} \cdot \vec{k} \end{aligned} \right\} \quad (2.4)^{++}$$

$$\left. \frac{\partial \phi^{*}}{\partial z^{*}} \right|_{z^{*} = -(1 + \vec{D}(t) \cdot \vec{k}) / \ell}$$

where gravity acts in the negative z -direction, ϕ is the velocity potential η is the displacement of the free surface from equilibrium, \vec{i} and \vec{k} are unit vectors in the x and z -directions and $x^{*} = x/\ell$, $z^{*} = z/\ell$, $\eta^{*} = \eta/\ell$,

[†]For a discussion of the dimensional equations, see Reference 2.

⁺⁺These equations represent the kinematic free surface boundary condition (2.2), the dynamic free surface boundary condition (2.3), and the solid wall boundary conditions (2.4).

$$\tau = t/\sqrt{l/g}, \quad \phi^* = \phi/\sqrt{l^3/g}, \quad \vec{v}^* = \vec{i} \frac{\partial}{\partial x^*} + \vec{k} \frac{\partial}{\partial z^*}.$$

To guarantee similitude in Equations 2.1 through 2.4, we must require

$$P(x, t) = \rho g l P^*(x^*, \tau) \quad (2.5)$$

and

$$\vec{D}(t) = l \vec{D}^*(\tau), \quad (2.6)$$

Thus, if a fluid-container system of characteristic length l_1 , is subjected to an overpressure $P_1(x, t)$ and a displacement $\vec{D}_1(t)$, a geometrically similar fluid-container system of characteristic length l_2 will undergo dynamically similar motion provided

$$\vec{D}_2(t) = (l_2/l_1) \vec{D}_1(t \sqrt{l_1/l_2}) \quad (2.7)$$

and

$$P_2(x, t) = (l_2/l_1) P_1(x l_1/l_2, t \sqrt{l_1/l_2})^\dagger. \quad (2.8)$$

With viscous, surface tension, and compressible effects neglected, Equations 2.7 and 2.8 completely specify the ground motion and overpressure scaling requirements, and in the idealistic situation where complete control over the environment is feasible, no more need be said. Unfortunately, complete environmental control is not always possible, especially when HE field tests are used to model prototype response. For example, although HE and NE ground motion waveforms are reasonably similar (and hence Equation 2.7 can be satisfied by adjusting the length scale and range from ground zero), the spatial and temporal dependence of overpressures generated by explosions of different yields is inconsistent with the

[†]The position $x = 0$ is defined as the leading edge of the container.

requirements of Equation 2.8. This fact has lead to the development of approximate overpressure scaling rules which are useful under limiting circumstances.

2.2 Overpressure Impulse Scaling

If the overpressure positive phase duration is small compared to the period of the lowest fluid response mode and effects of the negative phase are negligible, the analysis presented in Section 3 (see Equation 3.13) demonstrates that with regard to airblast-induced fluid motion, positive phase impulse gradient is the most important overpressure parameter. Integrating Equation 2.8 over time, we obtain the scaling relation

$$I_2(x) = (\ell_2/\ell_1)^{3/2} I_1(x\ell_1/\ell_2), \quad (2.9)$$

where I denotes positive phase overpressure impulse. If P is the peak overpressure at $x = 0$, R is the radius from ground zero and W is the explosive yield; impulse scaling is obtained through the following steps:

1. Since $I \sim P^{1/2} W^{1/3}$ provided $P \lesssim 1000$ psi (see Ref 3), Equation 2.9 requires $P^{1/2} W^{1/3} \sim \ell^{3/2}$.
2. The geometrical requirement specified by the function arguments in Equation 2.9 is satisfied if $R \sim \ell$.
3. The relation $P \sim (W^{1/3}/R)^n$ (where $2 \lesssim n \lesssim 3$ for $P \gtrsim 10$ psi) together with (1) and (2) implies that $P \sim \ell^j$, $\ell \sim W^m$, where $j = 1/(1+2/n)$ and $m = 2/3(3-j)$, i.e., $1/2 \leq j \leq 3/5$ and $5/15 \leq m \leq 5/18$.

For fixed P , $P \sim W^{1/3}$ and the impulse gradient ($\sim I/P$) exhibit a negligible yield dependence. Thus, the only explicit scaling rule is $P \sim \ell^j$, although there is an implicit yield dependence because we have assumed that the positive phase duration is small compared to the lowest mode period. For very large yields and/or very small containers, this type of scaling is inappropriate (e.g., impulse scaling is accurate if $W^{1/3}/T \ll 1$, where W is expressed in MT and T is the lowest mode period in seconds). Since the fundamental periods for containers with lengths of

100-300 ft vary from 5-15 sec, the use of impulse scaling for yields > 1 MT could lead to inaccuracies. For situations where this condition is violated, and the yield is not sufficiently large for $W^{1/4}$ scaling (see below) to apply, or when the effects of a negative phase are of interest, no simple scaling rule applies, and a more detailed examination of the problem is necessary.

2.3 Quarter Root of Yield Scaling

The scaling requirements, $P \sim \ell$ and $\ell \sim W^{1/4}$, commonly referred to as quarter root of yield scaling, are derived in Reference 4 with the aid of the strong shock relations $W \sim PR^3$ and $u(\text{shock speed}) \sim P^{1/2}$, under the assumption that the characteristic time scale for the problem is the air shock transit time across the container.

If the positive phase duration is much longer than the container's lowest mode period, $W^{1/4}$ scaling is applicable because the important forces are applied to the fluid surface only during the air shock traverse (and hence the transit time does serve as a characteristic time scale). On the other hand, in cases where the positive phase duration is short, important forces are applied to the surface long after the air shock front has passed (when the overpressure decay time constant is unrelated to the shock transit time). Unfortunately, $W^{1/4}$ scaling appears to be appropriate only for extremely large yields and/or very small containers. For container lengths on the order of a few hundred feet, this scaling is not accurate unless the yield $\gtrsim 100$ MT.

2.4 Ground Motion Scaling

For a given $\vec{D}_1(t)$, Equation 2.7 defines a $\vec{D}_2(t)$, which will preserve dynamic similarity of the fluid motion. Laboratory experiments can, in principle, satisfy Equation 2.7 to any desired degree of accuracy; therefore, prototype waveforms can be accurately modeled--to the extent that they are known. From the standpoint of field tests, ground motion scaling is approximate because of difficulties in precisely scaling HE and NE ground motion waveforms. However, a well-designed HE experiment provides a

3
wide variety of ground motion environments which usually model some nuclear waveforms of interest.

If the dominant frequency of a prototype displacement waveform is f_p , and the dominant frequency of a field test waveform is f_t , the length scale which should be used in the field test is determined from Equation 2.7 as

$$\frac{l_t}{l_p} = \left(\frac{f_t}{f_p} \right)^{-2},$$

where l_p is the prototype length scale.

Thus, for field test experiments, ground shock scaling requirements can be satisfied fairly accurately, but only at the expense of the overpressure requirements. This condition, coupled with the fact that rigorous scaling of overpressure effects is often impossible, strongly suggests that we attempt to understand fluid response from first principles, rather than totally relying on information from approximately scaled experiments. Consequently, in the next section, we present a more detailed analysis of fluid response to ground shock and overpressure.

SECTION 3

DYNAMICS OF FLUID RESPONSE TO GROUND MOTION AND OVERPRESSURE

3.1 Formulation

In this section, a normal mode analysis is used to examine the problem illustrated in Figure 1.1. Since the technique of modal decomposition can be applied to any fluid-container system excited in an arbitrary direction, the extension of these rectangular trench results to more complicated situations is straightforward.

Consider a two-dimensional, rectangular container of length l in the x -direction in a gravitational field g which acts in the negative z -direction. Suppose that the equilibrium fluid depth in the container is d and that the sides of the container are extended sufficiently to prevent any fluid loss.

With viscosity, surface tension, and compressibility neglected, Equations 2.1 through 2.4 and the initial conditions $\eta(0)=\dot{\eta}(0)=0$ comprise a boundary-initial value problem with a (presumably) unique solution. Unfortunately, the highly nonlinear nature of the problem precludes the use of simple solution techniques, although it is possible to obtain a useful approximate solution by linearizing Equations 2.2 through 2.4--i.e., we assume that the free surface and ground displacements are small compared to container dimensions and that the particle velocities are small compared to typical surface wave speeds. These assumptions are justified for most cases of interest, and even in situations where this is not so, the linearized solution is at least qualitatively useful.

The linearized, dimensional versions of Equations 2.2 through 2.4 are

$$\frac{\partial \phi}{\partial z}(x, 0, t) = \frac{\partial \eta}{\partial t}(x, t) \quad (3.1)$$

$$\frac{\partial \phi}{\partial t}(x, 0, t) + g\eta(x, t) + \frac{P(x, t)}{\rho} = 0, \quad (3.2)$$

$$\left. \begin{aligned} \frac{\partial \phi}{\partial x}(0, z, t) &= \frac{\partial \phi}{\partial x}(l, z, t) = \dot{D}(t) \\ \frac{\partial \phi}{\partial z}(x, -d, t) &= \dot{H}(t) \end{aligned} \right\} \quad (3.3)$$

which together with $\nabla^2 \phi = 0$ and the aforementioned initial conditions comprise the linearized problem. Here, $D(t)$ and $H(t)$ respectively are the horizontal and vertical components of the ground displacement.

In terms of ψ , defined by

$$\phi = \dot{D}(t)\left(x - \frac{l}{2}\right) + \dot{H}(t)z + \psi$$

the governing equations become

$$\nabla^2 \psi = 0 \quad (3.4)$$

$$\frac{\partial \psi}{\partial t}(x, 0, t) + (g + \ddot{H}(t))\eta(x, t) + \frac{P(x, t)}{\rho} + \ddot{D}(t)\left(x - \frac{l}{2}\right) = 0 \quad (3.5)$$

$$\dot{H}(t) + \frac{\partial \psi}{\partial z}(x, 0, t) = \frac{\partial \eta}{\partial t}(x, t) \quad (3.6)$$

$$\left. \begin{aligned} \frac{\partial \psi}{\partial x}(0, z, t) &= \frac{\partial \psi}{\partial x}(l, z, t) = 0 \\ \frac{\partial \psi}{\partial z}(x, -d, t) &= 0 \end{aligned} \right\} \quad (3.7)$$

Since the crater-induced vertical accelerations are usually small compared to g , $\ddot{H}(t)$ will be omitted from Equation 3.5 for the remainder of this section. Section 4 discusses the effect of this term under more general circumstances. Note that $\dot{H}(t)$ in Equation 3.6 only requires the equilibrium position of the free surface to move vertically with the displacement $H(t)$.

Equations 3.4 through 3.7, with all vertical motion terms omitted can be satisfied by setting

$$\psi = \sum_{n=1}^{\infty} A_n(t) \cos\left(\frac{n\pi x}{l}\right) \cosh\left(\frac{n\pi}{l}(z+d)\right) / \cosh\left(\frac{n\pi d}{l}\right)$$

$$\eta = \sum_{n=1}^{\infty} B_n(t) \cos\left(\frac{n\pi x}{l}\right)$$

where

$$\dot{A}_n(t) + g B_n(t) = \ddot{D}(t) \alpha_n + \beta_n(t) \quad (3.8)$$

$$A_n(t) \left(\frac{n\pi}{l}\right) \tanh\left(\frac{n\pi d}{l}\right) = \dot{B}_n(t) \quad (3.9)$$

with α_n and β_n defined by

$$(x-l/2) = - \sum_{n=1}^{\infty} \alpha_n \cos(n\pi x/l)$$

(i.e., $\alpha_n = 4l/(\pi n)^2$ for odd n ; $\alpha_n = 0$ for even n).

$$P(x,t) = - \sum_{n=1}^{\infty} \beta_n(t) \cos(n\pi x/l)$$

$$(i.e., \beta_n(t) = \frac{2}{\rho l} \int_0^l P(x,t) \cos\left(\frac{n\pi x}{l}\right) dx).$$

Elimination of A_n from Equations 3.8 and 3.9 yields

$$\ddot{B}_n + \omega_n^2 B_n = \frac{\omega_n^2}{g} [\ddot{D} \alpha_n + \beta_n] \quad (3.10)$$

where

$$\omega_n = [(n\pi g/l) \tanh(n\pi d/l)]^{1/2}$$

is the natural radian frequency of n^{th} normal mode. Equation 3.10 can be interpreted as describing the displacement of a harmonic oscillator of frequency ω_n , which is excited by the force $(\omega_n^2/g)(\ddot{D}\alpha_n + \beta_n)$. The solution of Equation 3.10, which satisfies the initial conditions $B_n(0) = \dot{B}_n(0) = 0$, is

$$B_n(t) = \frac{\omega_n^2 \alpha_n}{g} \left\{ D(t) - \omega_n \int_0^t D(\tau) \sin(\omega_n[t-\tau]) d\tau \right\} + \frac{\omega_n}{g} \int_0^t \beta_n(\tau) \sin(\omega_n[t-\tau]) d\tau, \quad (3.11)$$

where $t=0$ marks the start of the initial disturbance (either ground motion or overpressure). By differentiating Equation 3.11 and substituting the results into Equation 3.9, one can calculate $\Lambda_n(t)$ and thereby determine the fluid velocity field, $\vec{\nabla}\psi$.

The extension of Equations 3.10 and 3.11 to fluid-container systems with more complicated geometries is accomplished by replacing ω_n with the actual natural frequencies of the system in question and the modal functions $\cos(n\pi x/\ell)$ by the true mode shapes, which may be functions of two horizontal space variables. Note that this replacement changes the definitions of α_n and β_n . In laboratory experiments, the first few ω_n can be measured easily, whereas the mode shapes, with the possible exception of the first, are probably very difficult to determine. Fortunately, ground shock simulation experiments (to be discussed in Section 5) indicate the existence of a good correlation between fluid loss and the maximum virtual[†] waveheight associated with the first mode alone. Thus,

[†]Since the calculation of $B_n(t)$ assumes that fluid cannot leave the container, these waveheightsⁿ are termed virtual.

for fluid loss prediction, the first mode response appears to be the most important.

If ground motion effects are ignored, Equation 3.11 reduces to

$$B_n(t) = - \frac{2\omega_n}{\rho g l} \left\{ \int_0^l \cos\left(\frac{n\pi x}{l}\right) \int_0^t P(x, \tau) \sin(\omega_n(t-\tau)) d\tau dx \right\} \quad (3.12)$$

3.2 Fast Decay Approximation

If the modal periods are long compared to the positive phase duration D^+ (i.e., $(2\pi/\omega_n) \gg D^+$), Equation 3.12 can be approximated by

$$B_n(t) = \frac{-2\omega_n \sin(\omega_n t)}{\rho g l} \int_0^l I(x) \cos\left(\frac{n\pi x}{l}\right) dx,$$

where $I(x)$ is the positive phase impulse, and the effects of a negative phase have been ignored (the negative phase impulse is much smaller than the positive phase impulse when $P \gtrsim 100$ psi). Since

$$\frac{I(R+x)}{I(R)} \approx \left(\frac{P(R+x)}{P(R)} \right)^{1/2} \approx \left(\frac{R}{R+x} \right)^{3/2} \approx 1 - \frac{3x}{2R}$$

is a good approximation for yields and overpressure of interest [2],

Equation 3.12 can be further approximated by

$$B_n(t) \approx \begin{cases} -6 \left(\frac{l}{n\pi} \right)^2 \frac{\omega_n}{\rho g l} \frac{I(R)}{R} \sin(\omega_n t), & n \text{ odd} \\ 0, & n \text{ even.} \end{cases} \quad (3.13)$$

Equation 3.13 indicates that the surface response is dominated by overpressure impulse gradient ($\sim I(R)/R$). If impulse gradient scaling rules are employed, dynamic similarity of the fluid motion is guaranteed provided $(2\pi/\omega_n) \gg D^+$.

3.3 Step Wave Approximation

In the other extreme, $2\pi/\omega_n \ll D^+$, and the overpressure can be approximated by a step function:

$$P(x,t) = \begin{cases} 0 & 0 \leq t \leq x/u \\ P_0 & t \geq x/u, \end{cases} \quad (3.14)$$

where u is the air shock propagation velocity. Substitution of Equation 3.14 into Equation 3.12 gives

$$B_n(t) = \begin{cases} -\frac{8}{\pi} \frac{P_0}{\rho g l} \left(\frac{l}{n}\right) \frac{T_t}{T_n} \sin(\omega_n t), & n \text{ odd} \\ 0, & n \text{ even} \end{cases} \quad (3.15)$$

where $T_t = l/u$ is the shock transit time and $T_n = 2\pi/\omega_n$. The similitude properties of Equation 3.15 are consistent with $W^{1/4}$ scaling, which requires $P \sim l$ and assumes that $u \sim P^{1/2} \sim l^{1/2}$.

SECTION 4

DYNAMIC PRESSURE AND VERTICAL GROUND MOTION EFFECTS

4.1 Kelvin-Helmholtz (K-H) Wave Generation

Sections 2 and 3 have been concerned with the somewhat idealized problem of overpressure and ground motion induced fluid response. Clearly, the high-speed, time-dependent air flowfield associated with airblast environments can also interact with the fluid free surface, exciting waves and possibly causing fluid loss in the process. Although this interaction is difficult to describe theoretically, progress can be made in assessing the significance of some of the more simple dynamic pressure effects.

A qualitative understanding of dynamic pressure effects can be obtained by ignoring many of the more complex phenomena which would otherwise render the problem intractable. For example, if we ignore the boundary layer and the inherent three-dimensionality of the flow-field, treat the problem as quasi-static, and assume that the deformation of the fluid surface is small, the resultant airflow-fluid interaction can be interpreted as a Kelvin-Helmholtz instability. These assumptions generally exaggerate the strength of the airflow-fluid interaction. In particular, boundary layer effects tend to reduce the effective air velocity; large free surface deformations induce flow separation and thereby limit the growth of surface instabilities; and the actual three-dimensional flow can relieve itself, laterally, around the wave disturbance.

Consider a steady, inviscid airflow over a small amplitude, sinusoidal surface. For subsonic conditions, the surface variations induce a pressure disturbance in the air given by

$$\delta P = -C_d Q_s \eta k, \quad (4.1)$$

where η is the amplitude and k the wave number of the surface deflection, Q_s is the unperturbed dynamic pressure associated with the airflow, and

C_d is a drag coefficient that depends on the flow's Mach number [5].

Following an approach used to describe airblast interactions with structures [6], we assume that Equation 4.1 can be extended to unsteady flow situations by setting

$$\delta P(x,t) = -\overline{C_d}(M_0)Q_s(t)\eta(x,t)k \quad (4.2)$$

where $Q_s(t)$ is now the time-dependent dynamic pressure, and $\overline{C_d}$ is an average drag coefficient, assumed to depend only on the initial ($t = 0$) Mach number M_0 .

The pressure fluctuations (4.2) can be incorporated into (3.5) by replacing $P(x,t)$ with $P(x,t) + \delta P(x,t)$. The net result of this procedure is to replace $\omega_n^2 B_n$ in Equation 3.10 with

$$\omega_n^2 \left[1 - \frac{\overline{C_d} Q_s(t)}{\rho g} \left(\frac{n\pi}{\ell} \right) \right] B_n.$$

Thus, as expected, the dynamic pressure effect (represented by Kelvin-Helmholtz instability) forces the modal frequencies to become time-dependent and possibly imaginary. As noted previously, vertical ground accelerations cause a similar effect.

4.2 Approximate Treatment of Kelvin-Helmholtz Wave Generation and Vertical Ground Motion

The discussions presented in Section 4.1 and 3.2 indicate that both Kelvin-Helmholtz instability and vertical ground motions modify the basic modal equations as follows:

$$\ddot{B}_n(t) + \omega_n^2 (1 + \xi_n(t)) B_n(t) = \frac{\omega_n^2}{g} \left[\ddot{D}(t) \alpha_n + \beta_n(t) \right], \quad (4.3)$$

where

$$\xi_n(t) = \begin{cases} -\frac{\overline{C_d} Q_s(t)}{\rho g} \left(\frac{n\pi}{l} \right) & \text{(Kelvin-Helmholtz)} \\ \frac{\ddot{H}(t)}{g} & \text{(Vertical Ground Motion).} \end{cases}$$

Denoting $B_n^*(t)$ as the solution

$$\ddot{B}_n^*(t) + \omega_n^2 B_n^*(t) = \frac{\omega_n^2}{g} [\ddot{D}(t) \alpha_n + \beta_n(t)]$$

subject to $B_n^*(0) = \dot{B}_n^*(0) = 0$, we note that the differential equation (4.3), together with these same initial conditions, is equivalent to the Volterra integral equation

$$B_n(t) = B_n^*(t) - \omega_n \int_0^t B_n(\tau) \xi_n(\tau) \sin(\omega_n[t-\tau]) d\tau. \quad (4.4)$$

The Neumann series solution to Equation 4.4

$$\begin{aligned} B_n(t) = & B_n^*(t) - \omega_n \int_0^t B_n^*(\tau) \xi_n(\tau) \sin(\omega_n[t-\tau]) d\tau \\ & + \omega_n^2 \int_0^t \xi_n(\tau) \sin \omega_n(t-\tau) \int_0^\tau (t') B_n^*(t') \sin(\omega_n[\tau-t']) dt' d\tau \\ & + \dots \end{aligned} \quad (4.5)$$

is useful if the dynamic pressure and vertical motion perturbations are small, in which case

$$B_n(t) \simeq B_n^*(t) - \omega_n \int_0^t B_n^*(\tau) \xi_n(\tau) \sin(\omega_n[t-\tau]) d\tau, \quad (4.6)$$

where $B_n^*(t)$ is given by Equation 3.11.

4.3 Application to the Kelvin-Helmholtz Mechanism

Usually $Q_s(t)$ can be approximated by [3]

$$Q_s(t) = Q_s^0 e^{-t/\theta}.$$

In many cases of interest, θ is much smaller than the periods of the first few normal modes, so that for the purposes of integration

$$\sin(\omega_n[t-\tau]) \simeq \omega_n(t-\tau),$$

and $B_n^*(\tau)$ can be approximated as

$$B_n^*(\tau) \simeq \tau V_n,$$

where V_n is a characteristic velocity. Equation 4.6 can then be approximated by

$$B_n(t) \simeq V_n t + V_n \frac{\overline{C_d} Q_s^0}{\rho g} \left(\frac{n\pi}{l} \right) \omega_n^2 \int_0^\infty (t-\tau) \tau e^{-\tau/\theta} d\tau \quad (4.7)$$

provided $\omega_n t \ll 1$ and $t \gg \theta$. The relative importance of the Kelvin-Helmholtz correction can be expressed in terms of the parameter

$$K_n = \frac{\overline{C_d} Q_s^0}{\rho g} \left(\frac{n\pi}{l} \right) (\omega_n \theta)^2. \quad (4.8)$$

Thus, if $K_n \ll 1$, the series solution Equation 4.5 is useful, and the influence of the K-H mechanism is minor; if $K_n \gg 1$, Equation 4.5 probably does not converge, and the K-H effect is probably significant. For most prototype environments $K_n \ll 1$, at least for the first few modes, which are most important with regard to fluid loss.

Since $K_n \sim (n\theta/l)^2$, K-H wave generation becomes increasingly more important for the higher modes, (until limited by surface tension or viscosity) and large θ (i.e., large yield) environments. Relatively speaking, the importance diminishes as container dimensions increase. This discussion of K-H wave generation ignores many important phenomena including boundary layer effects. Miles [7] has suggested a method of evaluating the K-H effect for steady, incompressible, boundary layer flow. As one might expect intuitively, his results indicate that the determination of Q_s^0 should not involve the free stream velocity, but rather a velocity more typical of the boundary layer. This effect would tend to reduce the interaction strength about one or two orders of magnitude. Miles' theory explains in part why the K-H mechanism is unimportant for low-speed, wind-water interactions.

Assuming one wished to study the K-H mechanism experimentally, proper scaling can be obtained by holding the parameter K_n constant. This can be accomplished by requiring

$$Q_s^0, M_o = \text{constant} \quad (4.9)$$

$$\theta \sim l.$$

Since $\theta \sim W^{1/3}$ for explosive tests, the second relation in Equation 4.9 implies that $l \sim W^{1/3}$.

Before leaving the subject of dynamic pressure effects, we should point out that fluid can be removed from pools without the appearance of large amplitude waves. Shock tube experiments [8] have indicated

that the air flow behind a shock wave can significantly erode the fluid surface via a shear interaction between the air and fluid. It appears that, under more realistic field test explosive conditions, shear erosion is much less significant. In any case, a suitable physical model of this effect has not yet been perfected.

4.4 Application to Vertical Ground Motion

Substitution of $\xi_n(\tau) = H(\tau)/g$ into Equation 4.5 gives

$$B_n(t) \approx B_n^*(t) - \omega_n \int_0^t \frac{\ddot{H}(\tau)}{g} B_n^*(\tau) \sin(\omega_n[t-\tau]) d\tau. \quad (4.10)$$

Often $H(\tau)$ and $D(\tau)$ are non-zero only in a time interval which is short compared to $2\pi/\omega_n$, at least for the first few modes. Under such circumstances, a good approximation to $B_n^*(t)$ is (see Equation 3.11)

$$B_n(t) \approx (\omega_n^2 \alpha/g) D(t).$$

So that Equation 4.10 can be approximated by

$$B_n(t) \approx \frac{\omega_n^2 \alpha_n}{g} \left\{ D(t) - \omega_n^2 \int_0^t \frac{\ddot{H}(\tau)}{g} D(\tau) (t-\tau) d\tau \right\}. \quad (4.11)$$

Note that the relative contribution to $B_n(t)$ from vertical motion depends on the phasing between the horizontal and vertical components. The relative importance of vertical motions is roughly represented by the size of the parameter

$$G = (\omega_n T)^2 \frac{\overline{\ddot{H}}}{g},$$

where T is the duration of the ground motion and $\overline{\ddot{H}}$ is some "average" vertical acceleration. Since $\omega_n T < 1$, the magnitude of typical vertical

accelerations must be somewhat larger than g if the vertical motion contribution to $B_n(t)$ is to be significant.

4.5 Summary

This analysis suggests that both vertical ground motion and K-H wave generation may be unimportant, particularly for large length scales. Estimates of K_n (see Equation 4.8) for typical prototype parameters and low mode numbers indicate that $K_n \ll 1$, especially if Miles' correction is applied. Unfortunately, the K-H mechanism is only a first-order approximation to the actual airflow-fluid interaction. Although there is reason to believe that under the highly transient conditions generated by a nuclear burst, K-H coupling probably overestimates the strength of the interaction, more effort is needed to clarify this point. Likewise, more effort should be devoted to the shear erosion effect described at the end of Subsection 4.3, and other wave generation mechanisms which are beyond the scope of this paper.

An examination of Equation 4.11 for typical ground motion waveforms indicates that the vertical motion correction is usually small. This observation appears to be consistent with the results of ground shock simulation experiments, which are discussed in Section 5.

SECTION 5

FIELD TEST AND LABORATORY GROUND SHOCK SIMULATION EXPERIMENTS

5.1 Introduction

Recently, several field and laboratory experiments have been performed to study blast and shock-induced fluid motion in small-scale containers. All containers were completely full at the start of each test, and the water loss was measured after each test.

On MIXED COMPANY III, a 500-ton tangent HE test, small-scale, fluid-filled containers (hereafter referred to as the MIXED COMPANY containers) were exposed to airblast, ground motion, and debris environments of varying severity [8]. These containers, which are illustrated in Figure 5.1, were placed at distances from ground zero ranging from 300 to 900 ft (corresponding to 250-10 psi peak overpressures). The results and preliminary interpretation of these experiments are given in Reference 9, and therefore will not be discussed here except to compare the results with fluid loss predictions.

Fluid loss observed on MIXED COMPANY III was induced by the combined action of airblast, ground shock and debris impact. To aid in unfolding the relative influence of these water loss mechanisms, laboratory experiments have been conducted to study fluid response to ground motions without the interference of other possible loss mechanisms. These experiments were conducted on a dual-axis hydraulic dynamic simulator, at Wyle Laboratories' Norco, California facility [10]. The primary test series exposed water-filled MIXED COMPANY containers to uni-axial (horizontal) and simultaneous bi-axial (horizontal and vertical) excitation. A test series employing somewhat larger containers with several different wall slopes was also conducted. Emphasis was placed on parametric studies that varied input waveform frequency, amplitude, duration and vertical-horizontal phasing. The experiments involving combined vertical-horizontal loading were somewhat complicated by the fact that, for moderate vertical motions, the water separated from the container and entered a gravitational free-fall stage. Under a combined airblast ground-shock environment, fluid separation probably would be prevented or at least inhibited by the forces

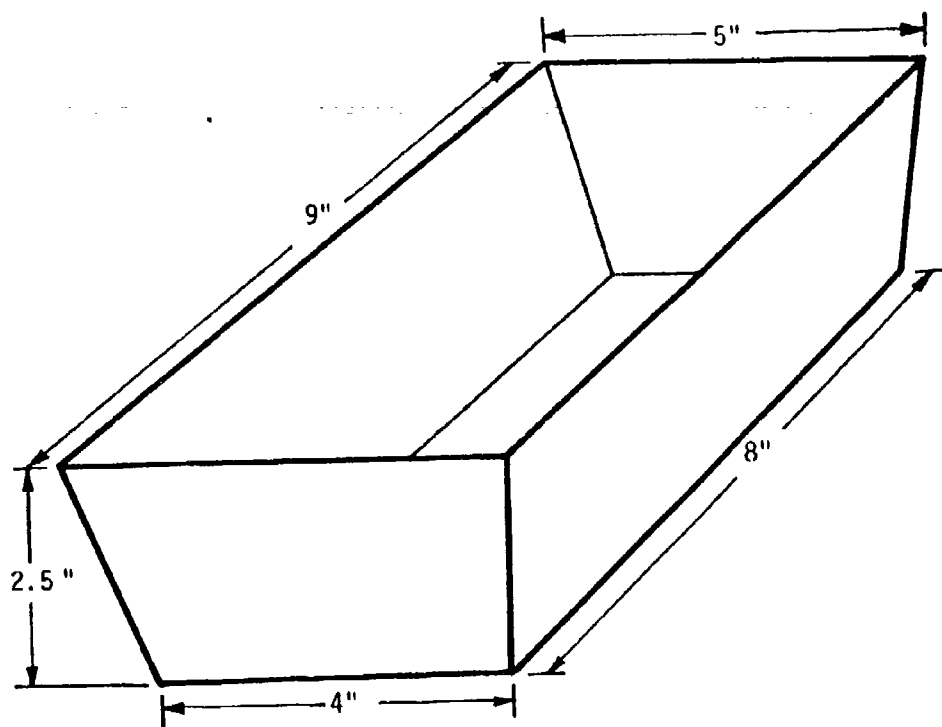


Figure 5.1 MIXED COMPANY Container

associated with the airblast overpressure. It is important to note that the theoretical approach to vertical motion effects presented in Subsection 4.5 cannot accommodate fluid-container separation. In any case, our efforts to develop a fluid loss prediction technique have been guided mainly by the single (horizontal) axis test results; consequently, only those results will be examined in detail.

5.2 Interpretation of Laboratory Experiments

From Equation 3.11, with $n = 1$, $\beta_n = 0$, the maximum "virtual" wave length h associated with the lowest mode is

$$h = \frac{4}{\pi} \tanh \left(\frac{\pi d}{\ell} \right) \text{MAX}_{0 < t < T} \left\{ D(t) - 2\pi f_o \int_0^t D(\tau) \sin(\omega_n[t-\tau]) d\tau \right\} \quad (5.1)$$

where ℓ is the container length in the direction of excitation, $D(t)$ is the input horizontal displacement waveform, T is the excitation duration, and f_o is the temporal frequency of the container's lowest normal mode.

The Wyle experiments employed a displacement waveform approximately represented by

$$D(t) = \begin{cases} a \sin(2\pi f t) & 0 < t < k/f \\ 0 & t > k/f \end{cases}$$

where $k = 1, 2$ or 3 . For the waveform expressed in Equation 5.2, Equation 5.1 can be expressed as

$$h = a \frac{4}{\pi} \tanh \left(\frac{\pi d}{\ell} \right) F_k(f_o/f) \quad (5.3)$$

where F_k must be determined numerically. A plot of $F_1(f_o/f)$ and $F_2(f_o/f)$ is presented in Figure 5.2. Note that the differences between the two functions are negligible except near resonance. The large values of F_2 calculated near resonance should be interpreted carefully because non-linear, wave-growth-limiting mechanisms were not considered in the analysis

presented in Section 3. Consequently, although the two-cycle fluid loss is expected to be larger than the one-cycle loss when $(f_0/f) \approx 1$, the difference is expected to be substantially less than indicated by Figure 5.2. This subject is somewhat academic for large amplitude ground motions near ground zero because they tend to have fewer cycles--often less than a complete cycle.

We expect that the observed depth loss Δd can be related in some manner to the maximum wave height achieved in response to the displacement excitation. Thus, we shall correlate the fluid loss data with the virtual wave height in Equation 5.3. For convenience, both the depth loss and wave height are normalized by the mean depth d . Figure 5.3 plots experimentally determined values of $\Delta d/d$ as a function of the theoretical virtual wave height h/d (i.e., $[a/d][4/\pi] \tanh [\pi d/\ell] F_1[f_0/f]$) for a single cycle displacement pulse (Equation 5.2 with $k = 1$). These data are from tests involving four container geometries (broadside and end-on MIXED COMPANY configurations, and broadside and end-on configurations for an 8" x 15" x 2" rectangular container) with $a/d = 0.1, 0.2, 0.3, 0.4$ for the MIXED COMPANY containers, and $a/d = 0.5$ for the other containers. In addition, several values of the input frequency f were investigated: $f = 1, 1.5, 2.5$ and 10 Hz for the MIXED COMPANY containers, and $f = 1, 2$, and 5 Hz for the 8" x 15" x 2" containers. The lowest mode natural frequencies for these containers are 2.37 and 1.55 Hz (broadside and end-on, MIXED COMPANY) and 1.55 and 0.90 Hz (broadside and end-on, 8" x 15" x 2" container).

To within the experimental scatter, $\Delta d/d$ appears to be proportional to h/d . This linear dependence is even more apparent if the data points where $f_0/f > 1$ are excluded, as shown in Figure 5.4. For container lengths on the order of 100 ft or larger and yields ≈ 50 MT, $f_0/f < 1$. Thus, the linear relationship between $\Delta d/d$ and h/d appears to be quite accurate in the nondimensional frequency domain of most practical concern.

On the basis of this data, we hypothesize that the fractional depth loss is related to the maximum wave height via

$$\Delta d/d = \Gamma h/d,$$

where $\Gamma = 0.31 \pm 0.02$ for rectangular containers and $f > f_0$.

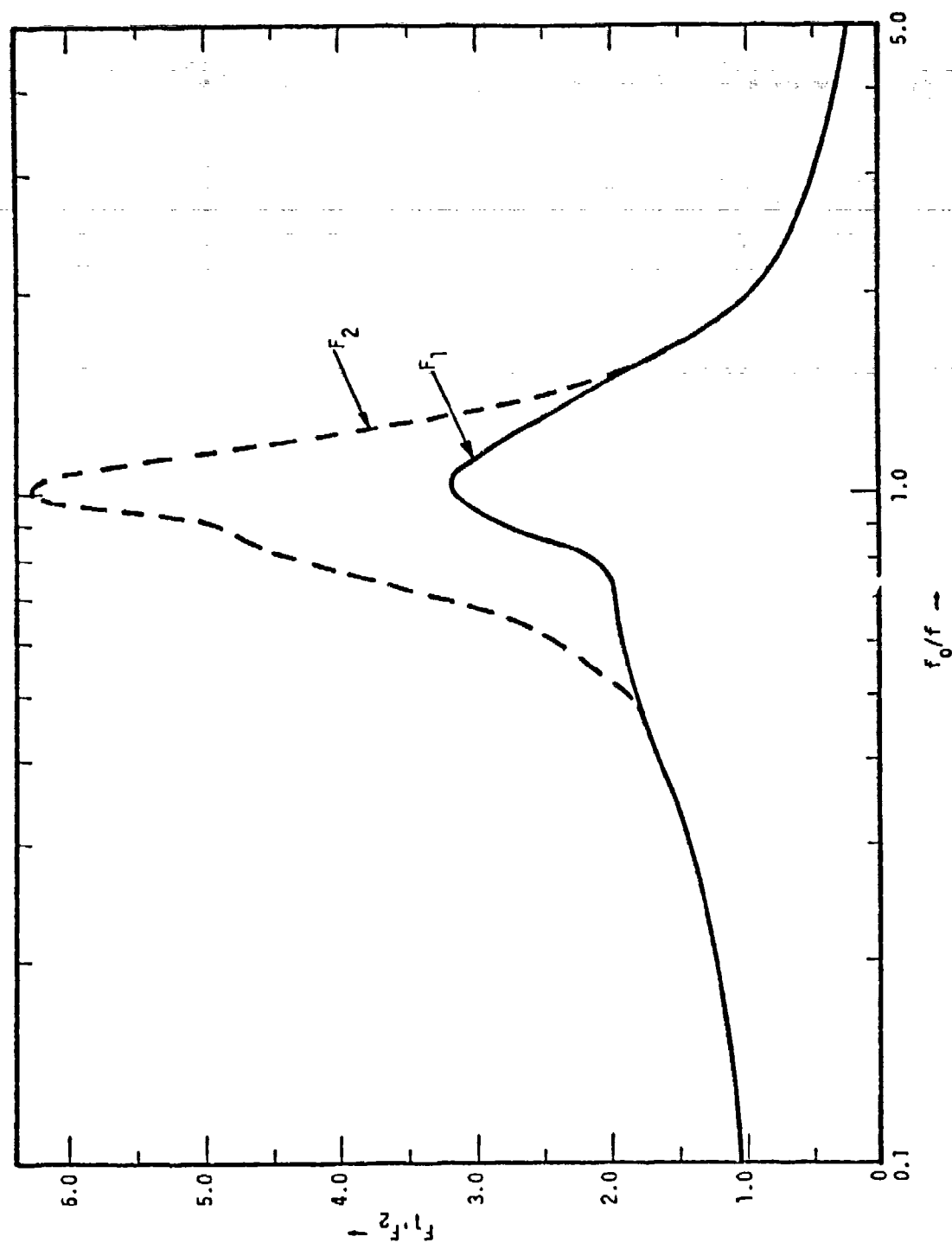


Figure 5.2. Maximum Wave Height Form Factor as a Function of Nondimensional Displacement Waveform Frequency

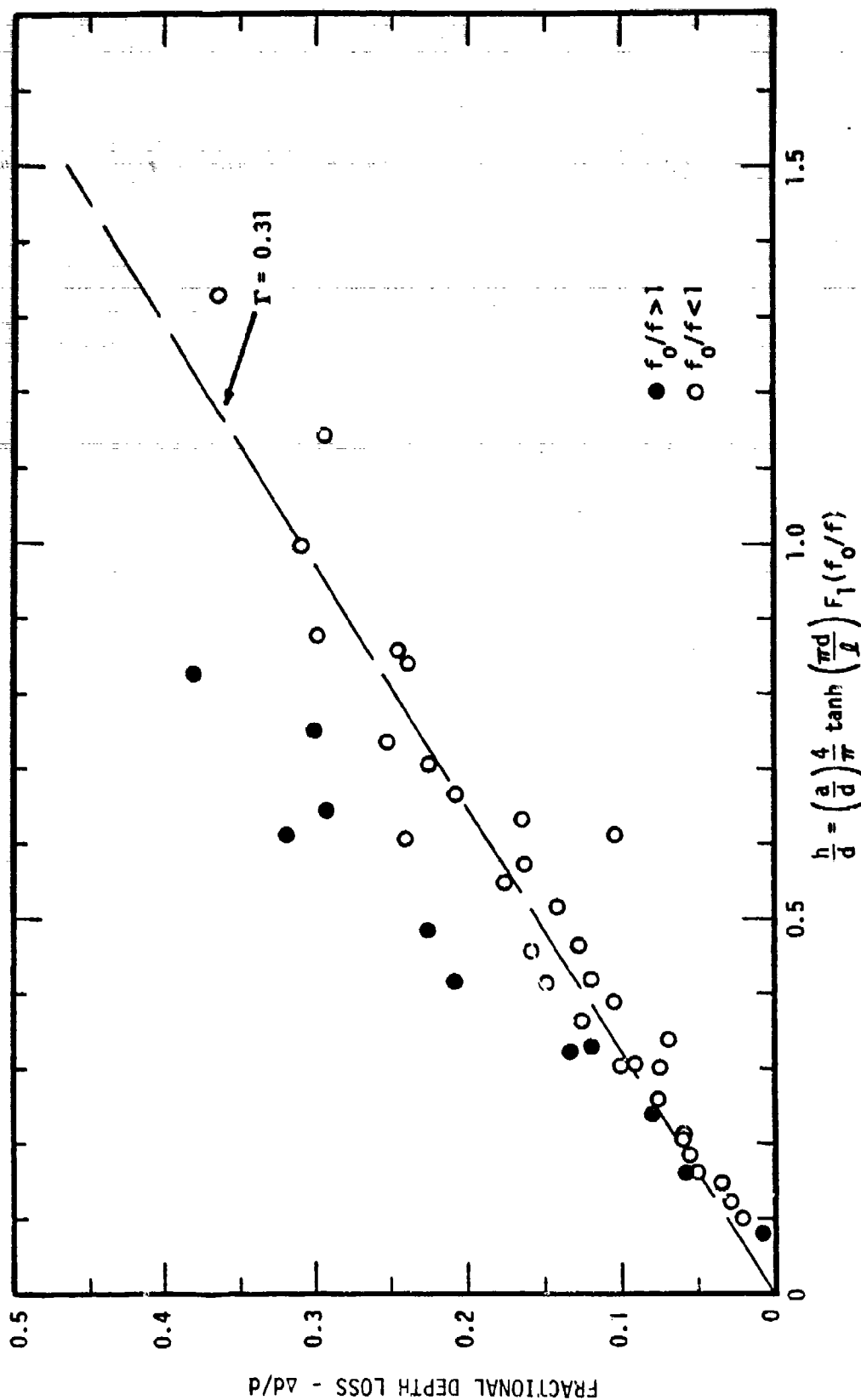


Figure 5.3 Fractional Depth Loss Measurements as a Function of Normalized Maximum Wave Height

To illustrate the implications of Equation 5.4, a more detailed view of the laboratory water loss data from the MIXED COMPANY containers (for the displacement pulse in Equation 5.2, with $k = 1$) is given in Figures 5.5 and 5.6. Also shown in these figures are predictions based in Equation 5.4 with h given by Equation 5.3 and $\Gamma = 0.31$.

The disagreement near resonance probably results from two effects. First, nonlinear effects limit wave height growth and tend to flatten the peak for relatively large values of a/d . Second, as fluid is lost from a container, the resonance frequency f_0 lowers--an effect that tends to broaden the resonance peak over a wider range of frequencies.

Experiments were also conducted with 8" x 15" x 2" rectangular containers that could be modified by inserts to vary the wall slopes. Although too few data were obtained to confidently determine the relation between water loss and input amplitude as a function of frequency and wall slope, the results appear to be compatible with the fluid loss prediction formula (Equation 5.4) where Γ decreases monotonically with decreasing wall slope. The natural frequency of the first mode also appears to decrease monotonically. However, the variation in Γ and f_0 appears to be rather minor for wall slopes greater than 18 degrees. For the minimum slope tested (18°), f_0 was lowered by about 15 percent from the natural frequency for rectangular containers, while Γ decreased at most by 25 percent from 0.31 to about 0.25.

5.3 Comparison with Field Test Data

The maximum "virtual" wave height associated with the lowest normal mode can, in principle, be calculated for any combined ground motion airblast environment. Equation 5.4, which was derived from experiments involving only ground motion loading, may then be assumed to predict fluid loss for combined airblast ground-shock environments. Although this assumption has not been verified through a comprehensive experimental program, it is intuitively appealing and will be used in the remaining analysis in this paper. Because dynamic pressure and vertical ground motion add complexity to any maximum wave height calculation, and because these effects are thought to be relatively unimportant, the

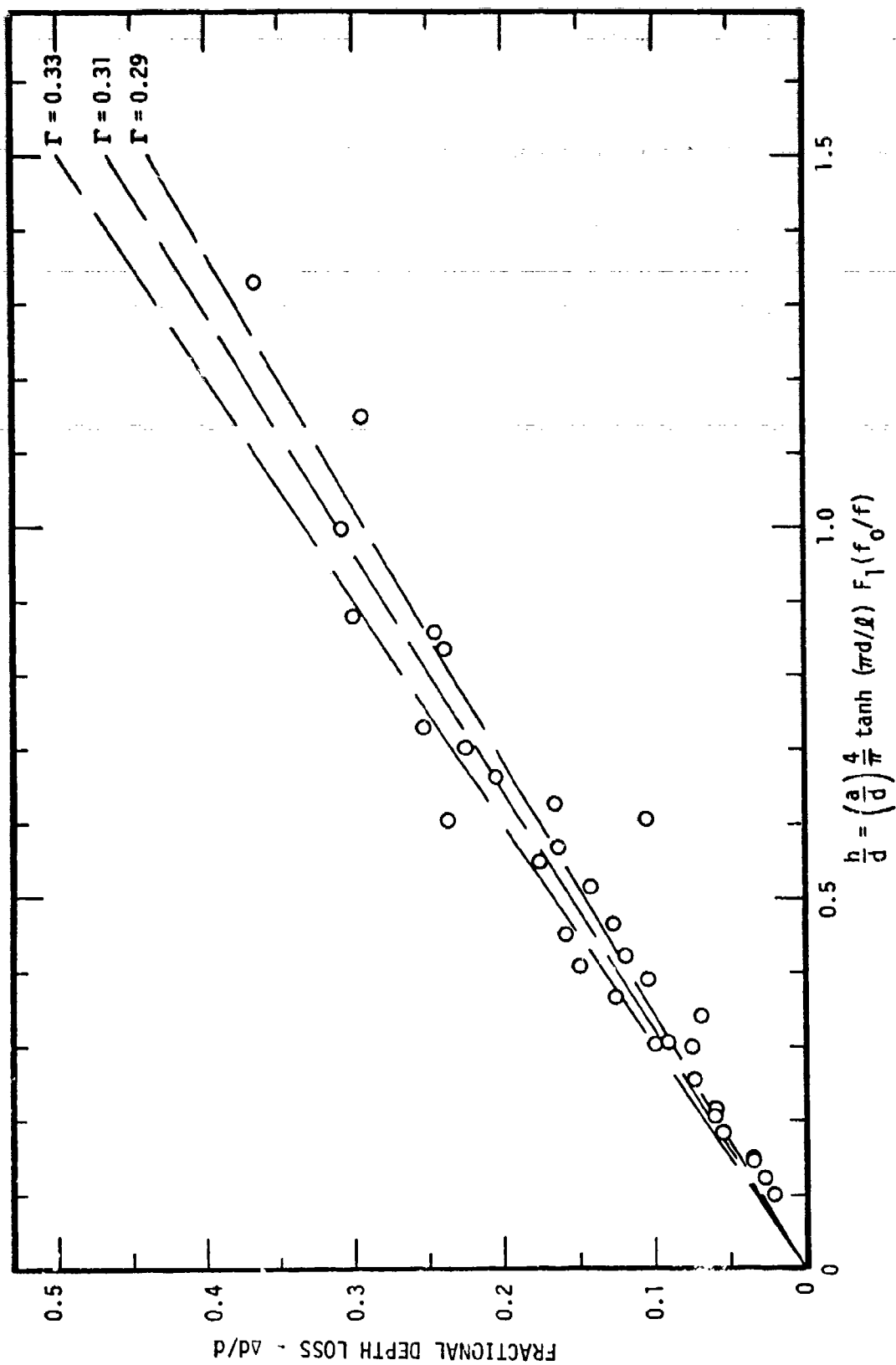


Figure 5.4 Fractional Depth Loss Measurements as a Function of Normalized Maximum Wave Height ($f_0/f < 1$)

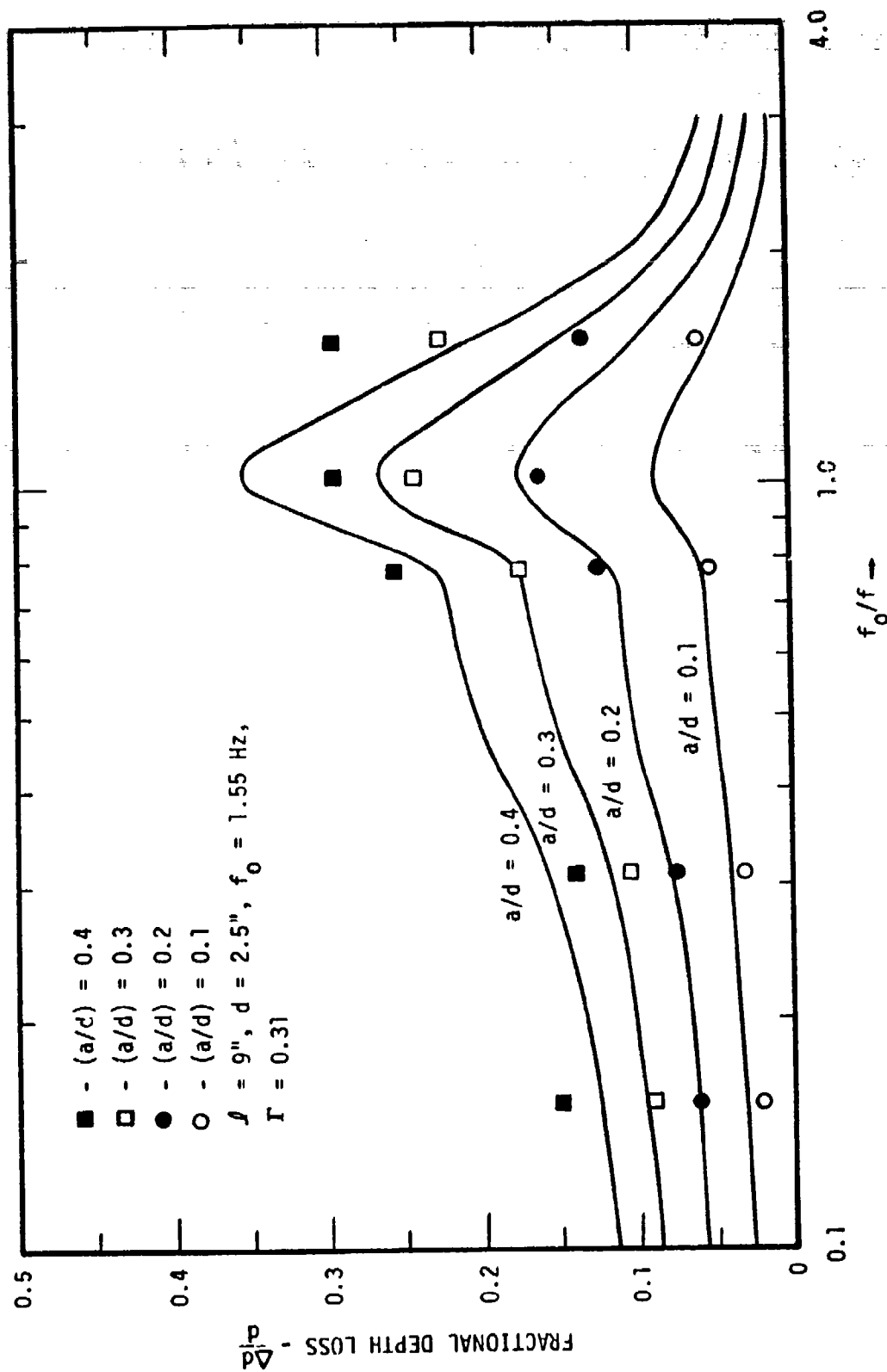


Figure 5.5 Fractional Depth Loss Predictions and Experimental Results as a Function of Nondimensional Frequency for Various Values of Nondimensional Input Displacement Amplitude

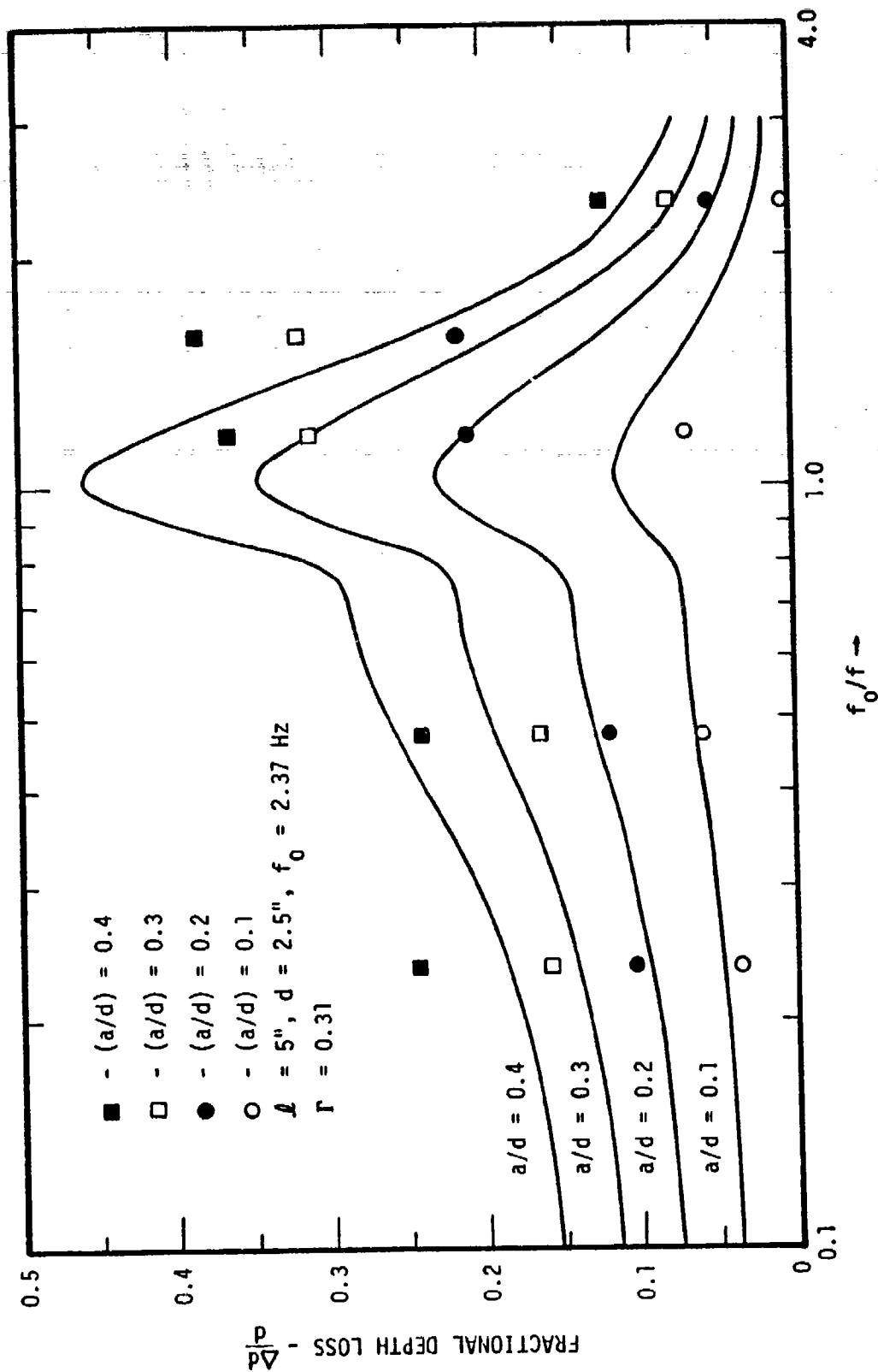


Figure 5.6 Fractional Depth Loss Predictions and Experimental Results as a Function of Nondimensional Frequency for Various Values of Nondimensional Input Displacement Amplitude

following calculations will only consider fluid loss caused by horizontal ground motion and overpressure loading. We shall show that such a prediction procedure is consistent with the field test observations on MIXED COMPANY [9]; thus demonstrating some confidence in applying this procedure to estimate water loss in prototype situations.

The horizontal low-frequency ground shock environment on MIXED COMPANY can be approximated by a sinusoidal displacement waveform of about one period in duration. The basic frequency of the waveform was about 5 Hz, and the measured attenuation of peak displacement with range from ground zero is given in Figure 5.7. Consequently, we shall model $D(t)$ as a one-cycle 5-Hz sinusoidal waveform exhibiting the attenuation characteristics given by the line in Figure 5.7. Since $f_o/f \lesssim 0.5$, the predictions are relatively insensitive to errors in this nominal frequency value.

For the following calculations, the overpressure time history is modeled as a sum of three exponentials:

$$\Delta P = P(1-\tau)(ae^{-\alpha\tau} + be^{-\beta\tau} + ce^{-\gamma\tau})^{\dagger}$$

where $\tau = (t-t_s)/D^+$, t_s is the time of shock arrival and D^+ is the positive phase duration. The parameters a , b , c , α , β , and γ are given as a function of peak overpressure in Reference 3. Although this overpressure approximation is valid only for nuclear environments, it can be a reasonable model for HE explosions provided the actual HE overpressures and positive phase durations are used. Accordingly, these data are taken from Reference 11. For simplicity, the ground shock and airblast arrival

[†] Here, $P(x)$ and $t_s = x/u$, where u is the approximately constant shock speed across the containers, are the only parameters treated as functions of position over the fluid's surface. All other parameters are taken to be independent of position, being functions of the reference overpressure $P(x=0)$, alone. This approximation is conservative because it tends to overestimate the overpressure positive phase impulse gradient across the container. More accurate overpressure models are currently being formulated.

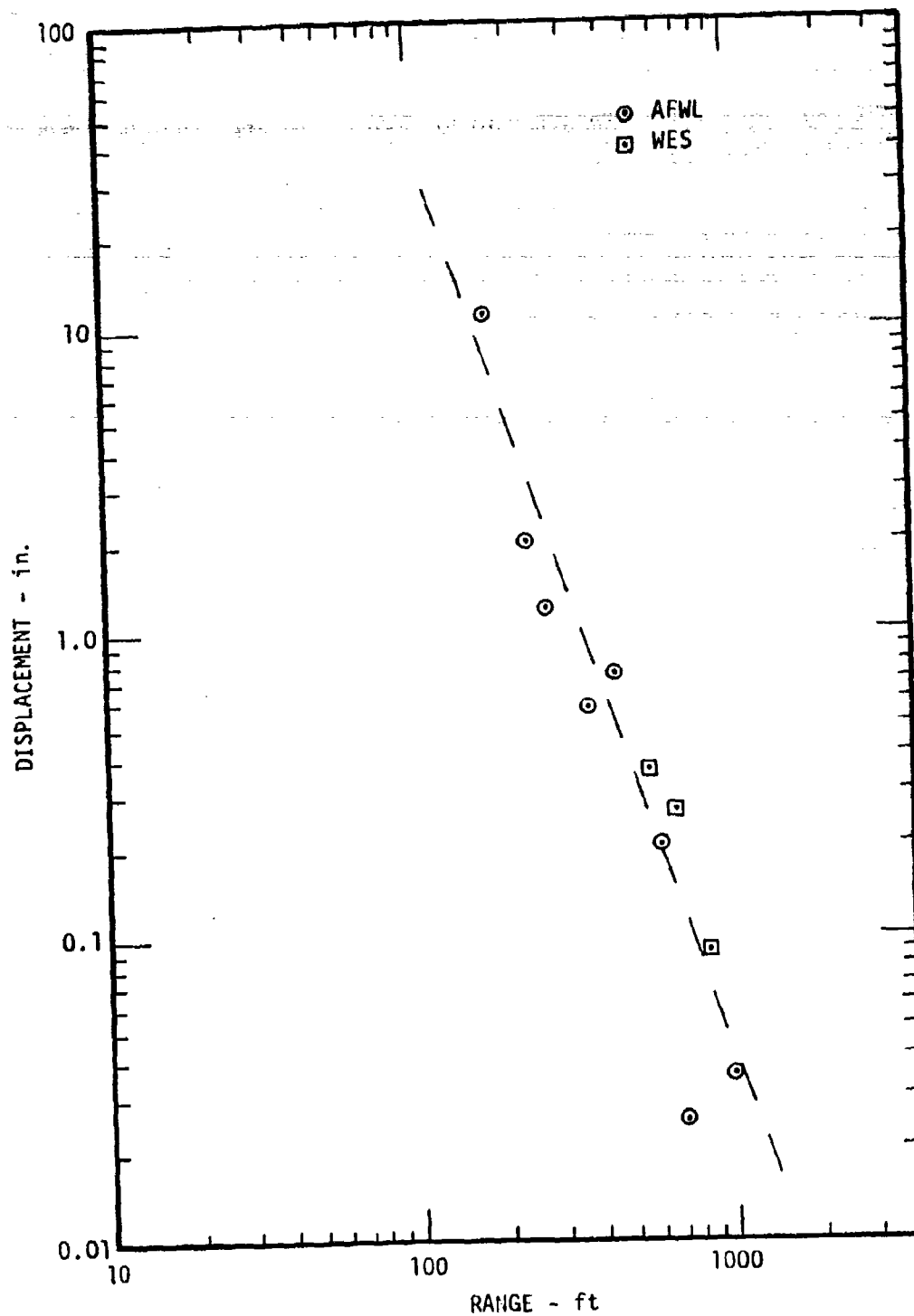


Figure 5.7 Peak Surface (1.5-ft depth) Horizontal Displacements on MIXED COMPANY

times are assumed to coincide. Only a small error (usually <10 percent in $\Delta d/d$) is introduced by this assumption.

Figure 5.8 compares the small container data with calculated water loss from combined airblast and horizontal ground motion loading. Vertical ground motion, debris impact, and dynamic pressure effects are ignored in this model. The theory does differentiate between broadside and end-on configurations; however, the differences are too small to indicate in Figure 5.8. The broadside configuration loses more fluid until the range exceeds about 700 ft, after which the end-on configuration loses more. The calculations appear to qualitatively describe the variation of fluid loss with range, although they generally underestimate the observed fluid loss.

Comparison of calculated results and laboratory experiments with the field experiments suggests that about half of the observed fluid loss from the small containers on MIXED COMPANY can be attributed to horizontal ground motion alone, provided the range from ground zero is less than about 450 ft. At ranges in excess of about 600 ft, the theory predicts that the airblast loading causes most of the fluid loss.

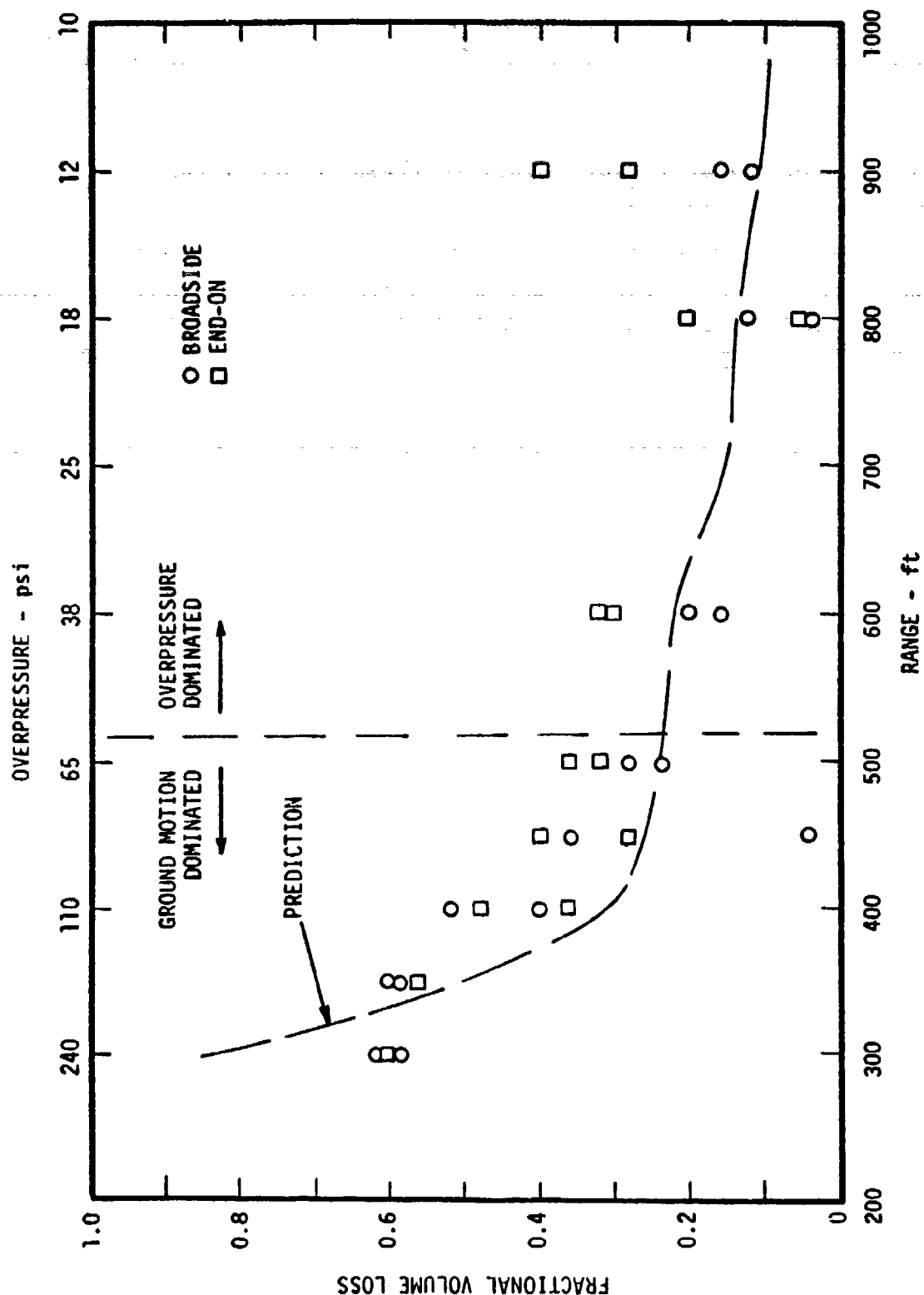


Figure 5.8 MIXED COMPANY Data and Predictions (Neglecting Vertical Ground Motion, Debris Impact and Dynamic Pressure Effects) for Small Containers

SECTION 6

PREDICTION OF FLUID LOSS IN A NUCLEAR ENVIRONMENT

6.1 Characterization of the Environment

The low-frequency ground motions from a near-surface explosion may be represented by a single-cycle displacement waveform whose amplitude is derived from

$$a \approx 0.45 V^{4/3}/R^3 \quad \text{for } R/V^{1/3} \lesssim 7.5 \quad (6.1)$$

where V is the apparent crater volume, and R is the range from ground zero. This assumption is based on the correlation of ground motion data from existing high-explosive and nuclear cratering explosions, and is referred to as the "crater volume" correlation within the U.S. ground shock community. Although the data analysis leading to Equation 6.1 has not been published in the unclassified literature, the crater volume correlation has been previously referred to in studies of ground shock in hard rock [12]. For $R/V^{1/3} \gtrsim 7.5$, Equation 6.1 is expected to underestimate the peak displacements which attenuate less rapidly at greater ranges. This fact, along with the observation that ground motions become more oscillatory with increasing range, leads us to believe that the following results underestimate water loss if $R/V^{1/3} \gtrsim 7.5$.

We estimate that $V \approx 2 \times 10^8 W \text{ ft}^3$ for wet soils, where W is the yield in megatons. For dry soils, we estimate that $V \approx 5 \times 10^7 W \text{ ft}^3$. Since for $P \gtrsim 100 \text{ psi}$,

$$P \approx 3750 W \left(\frac{1000}{R} \right)^3 \text{ psi}, \quad (6.2)$$

where R is the range in ft. Equations 6.1 and 6.2 can be combined with the assumption of a single-cycle sinusoidal waveform to obtain

$$D_w(t) \approx 8.3 W^{1/3} (P/600) \sin 2\pi f t \quad \text{wet soil}, \quad (6.3)$$

and

$$D_d(t) \approx 1.3 W^{1/3} (P/600) \sin 2\pi f t \quad \text{dry soil}. \quad (6.4)$$

Based on analysis of ground motion data from high-explosive and nuclear cratering tests in the Pacific, we estimate that

$$f \approx \kappa/W^{1/6} \text{ Hz,}$$

where $0.25 \lesssim \kappa \lesssim 1$.

For the following calculations, the overpressure, as in the previous chapter, is modeled after Brode [3], and the ground shock and air shock arrival times are again assumed to coincide. Debris impact, vertical motion and dynamic pressure are completely ignored.

6.2 Prediction Calculations

Figures 6.1 through 6.4 give predictions of fluid loss based on Equation 5.4, where the maximum wave height is calculated from Equation 3.11, for nuclear environments and rectangular contained geometries of interest. Figures 6.1 and 6.2 indicate the depth loss experienced under dry geologic conditions as a function of peak overpressure and yield. The container dimensions for the calculations are $\ell = 100$ ft, $d = 40$ ft in Figure 6.1, and $\ell = 300$ ft, $d = 40$ ft in Figure 6.2. The same information for wet geologic conditions is presented in Figures 6.3 and 6.4. The bands in these figures arise from the uncertainty in predicting the displacement waveform frequency. Generally speaking, the larger losses are associated with the lower frequency limit, $f = 0.25/W^{1/6}$; the lower losses with the higher frequency limit, $f = 1.0/W^{1/6}$. An exception to this rule is the 100 MT, $\ell = 100$ ft, predictions. In these cases, the lower frequency limit corresponds to $f_0/f \geq 1$, while for higher frequency limit, $f_0/f \leq 1$. Thus, an intermediate frequency actually is associated with the larger loss.

Because larger containers are less sensitive to ground motions than smaller containers, the $\ell = 300$ ft container generally loses less fluid than the $\ell = 100$ ft container. Figure 6.2 indicates that the sensitivity of fluid loss to yield is extremely low for the $\ell = 300$ ft container at low yields. In these cases, ground motion is relatively unimportant, and the overpressure is decaying quite rapidly relative to the normal mode period. Hence, Equation 3.13 should apply, and as mentioned in Section 2,

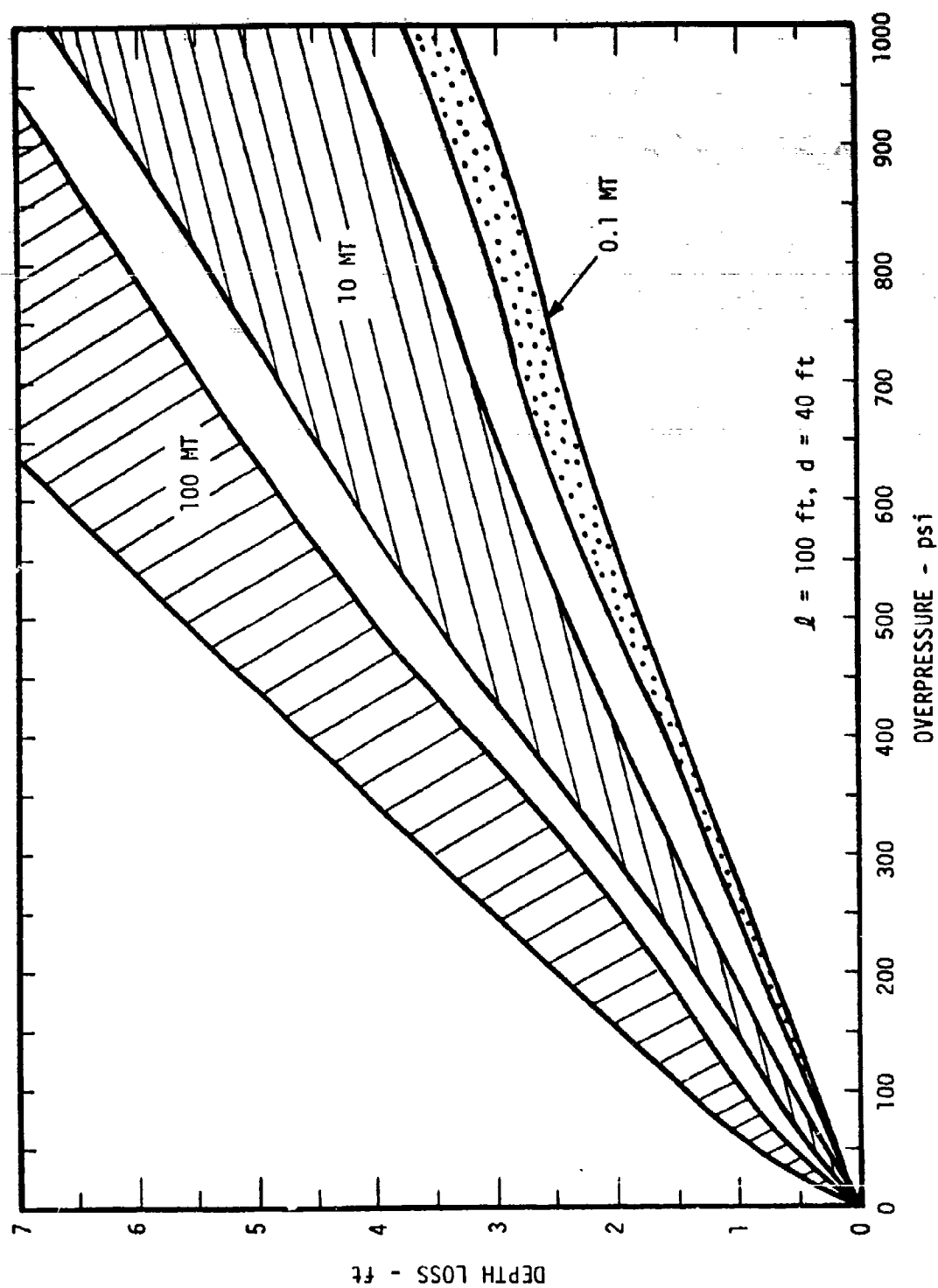


Figure 6.1 Predicted Depth Loss as a Function of Peak Overpressure and Yield for Dry Geologic Conditions

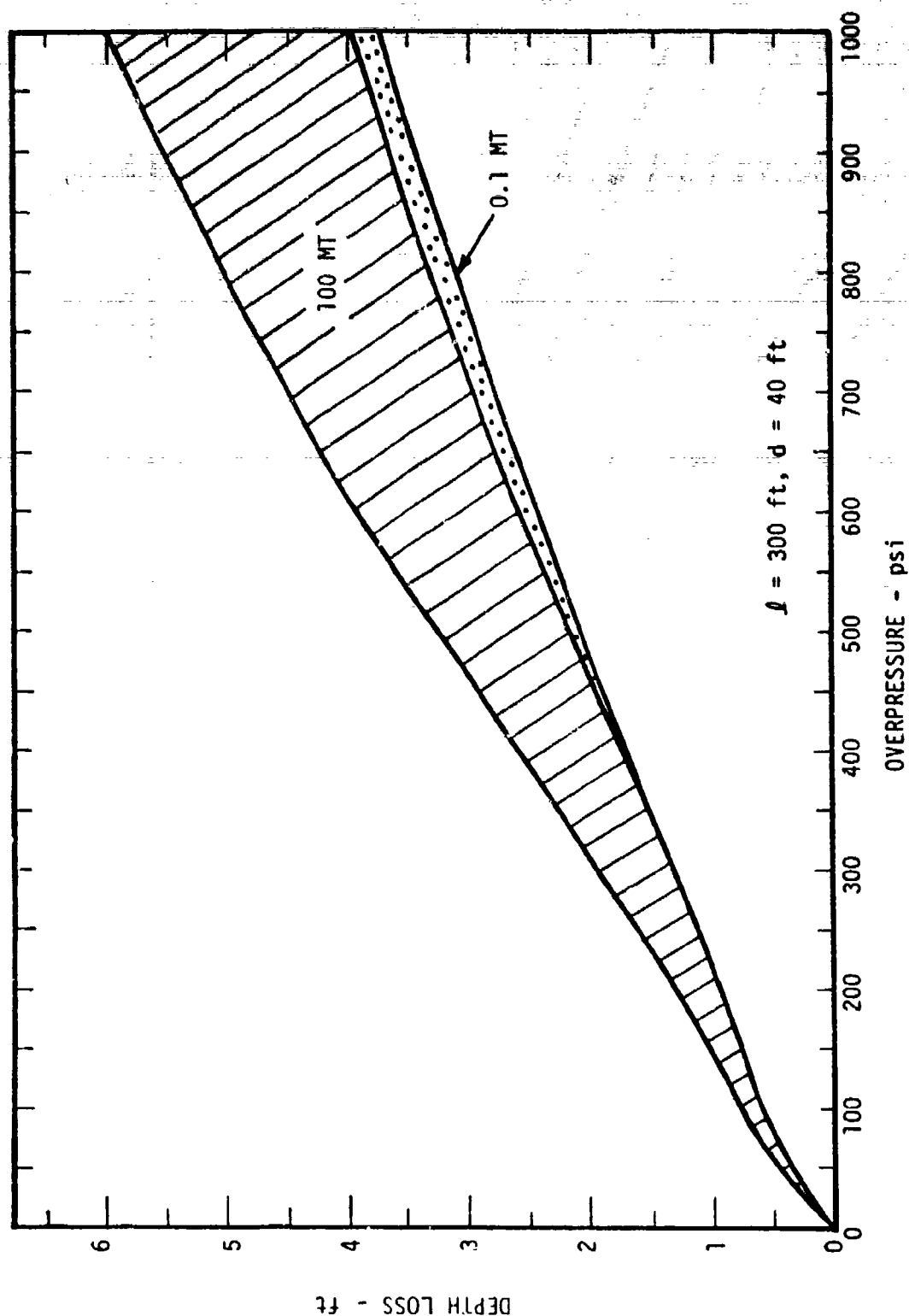


Figure 6.2 Predicted Depth Loss as a Function of Peak Overpressure and Yield for Dry Geologic Conditions

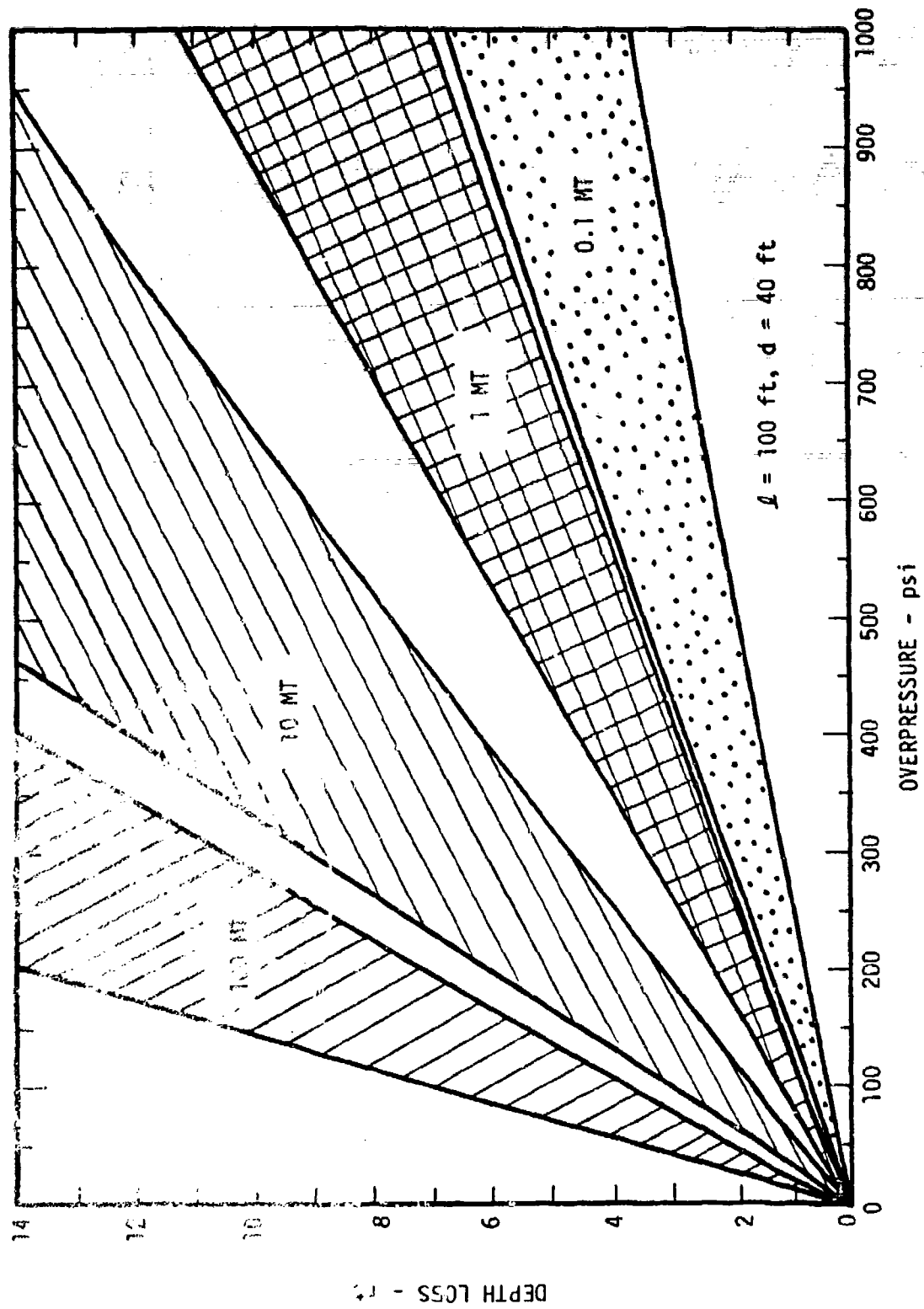


Figure 6.3. Predicted Depth Loss as a Function of Peak Overpressure and Yield for Wet Geologic Conditions

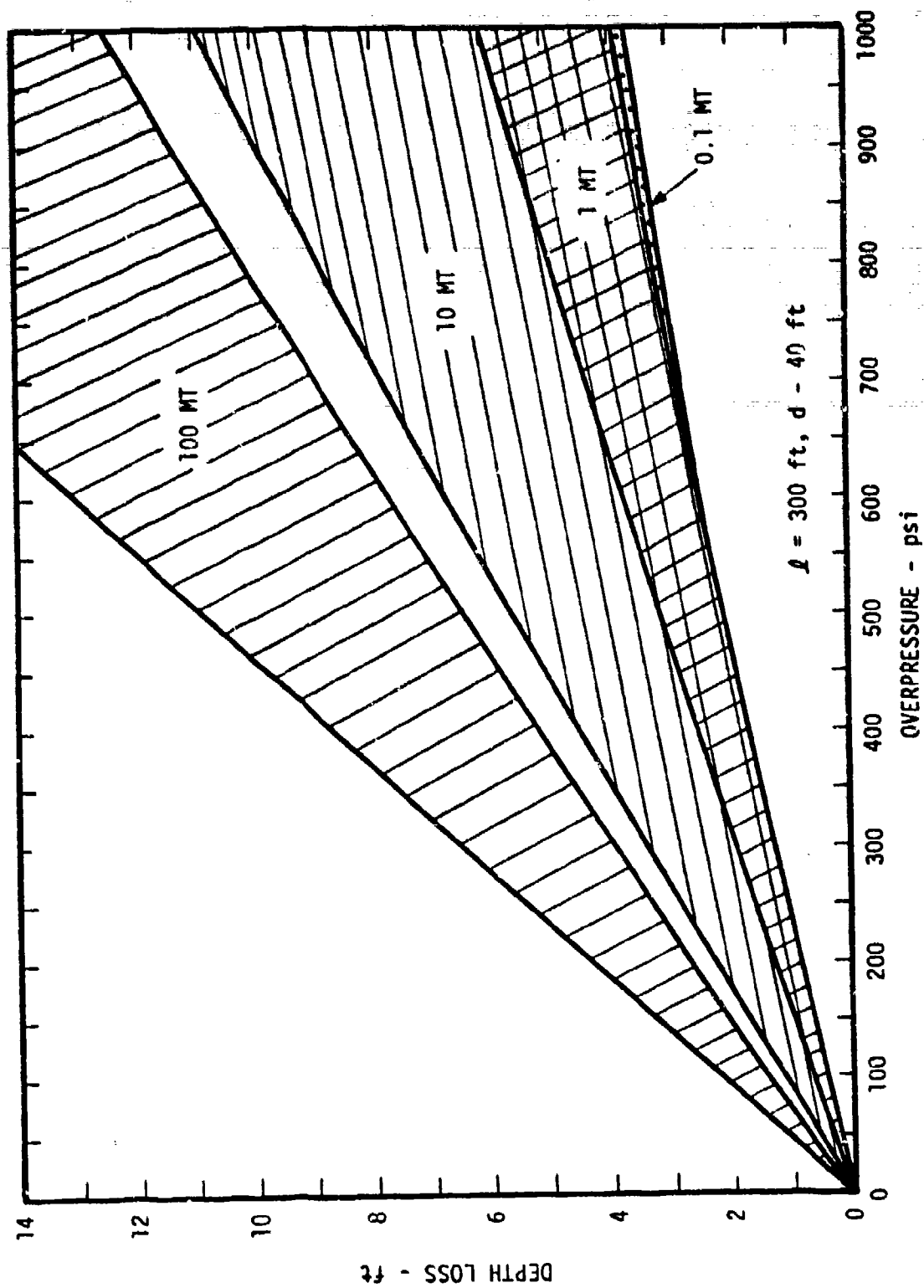


Figure 6.4 Predicted Depth Loss as a Function of Peak Overpressure and Yield for Wet Geologic Conditions

the wave height so determined is effectively yield-independent. Fluid loss from even large pools in wet geologies is usually dominated by ground motion.

The relative portion of fluid loss associated with ground motion varies considerably with the yield and container dimension variations presented in Figures 6.1 through 6.4. For the $l = 300$ ft configuration dry geologic conditions and low yields, the ground motion contribution is negligible, while the overpressure contribution is negligible for the $l = 100$ ft configuration and wet geologic conditions. The comparative danger associated with siting prototype systems in wet geologies is obvious from a comparison of Figures 6.1 and 6.3.

The fluid loss results presented in Figures 6.1 through 6.4, although valid only for rectangular containers, may be interpreted as a bounding estimate[†] of fluid loss from any sloped-wall container with a depth and maximum horizontal dimension given by the same d and l indicated in these figures. This fact follows from the observed wall slope dependence of Γ , discussed in Subsection 5.2.

Water loss from prototype trenches, canals, etc., may be prevented, or significantly reduced with the use of berms placed around their perimeters. As a practical matter, the cost of these berms would be nominal because excavated soil would be readily available for their construction. The wave height calculations discussed in this paper could be used to develop design criteria for berm features (e.g., berm height) once the threat environment and soil geology are specified.

[†]Provided vertical motion, dynamic pressure and debris impact are neglected.

SECTION 7

CONCLUSIONS AND SUMMARY

7.1 Scaling Requirements

Section 2 contains a discussion of scaling requirements that are applicable to the design of scaled experiments. In the absence of fluid compressibility, viscosity, surface tension and cavitation, the scaling laws for ground motion and airblast overpressure effects are given by Equations 2.7 and 2.8, respectively.

Application of these laws to high explosive field test experiments presents difficulties, however, since complete control over the environment is not possible. In fact, not only are the requirements of Equations 2.7 and 2.8 often mutually exclusive, but in addition, Equation 2.8 cannot be satisfied precisely. This observation led us to develop two approximate scaling requirements, one valid in the limit of large containers and/or small yields (Overpressure Impulse Scaling) and the other valid in the limit of small containers and/or large yields (Quarter Root of Yield Scaling). Impulse scaling is of more practical interest since most experimental parameters fall into its regime of validity.

7.2 Analytical Results

All analytical results presented here are obtained by linearizing the appropriate equations of motion and boundary conditions. This process is detailed in Equations (3.1) through (3.7). A modal description of fluid response to horizontal ground motion and overpressure loading culminates in Equation (3.11). In Subsection 3.2 a fast decay approximation for the overpressure contribution, (consistent with Impulse Scaling) is derived, while in Subsection 3.3 we present a stepwave approximation (consistent with Quarter Root of Yield Scaling).

In Section 4, we examine the inviscid coupling (Kelvin-Helmholtz) between a subsonic airflow and the fluid. An approximate correction to previously derived results to account for this interaction is contained

in Equation 4.7. It is demonstrated that the magnitude of the correction increases for higher mode numbers and large yield environments. Relatively speaking, its importance diminishes as container dimensions increase. Also presented in Section 4 is an approximate treatment of vertical ground motion effects.

7.3 Experimental Results

A discussion of laboratory ground shock simulation experiments is presented in Section 5. These experiments were conducted on a dual axis hydraulic dynamic simulator, and consisted of parametric studies that varied input waveform frequency, amplitude, duration and vertical-horizontal phasing. We observed a strong correlation between measured depth loss and maximum, calculated first mode waveheight, as indicated in Figure 5.3. The observed constant of proportionality for rectangular containers is approximately 0.3. Thus the data seem to be well-described by

$$\Delta d \approx 0.3h, \quad (7.1)$$

where Δd is the depth loss and h is the maximum first mode waveheight.

Equation (7.1) was assumed to hold for overpressure as well as ground motion environments, and predictions for the MIXED COMPANY fluid slosh experiments [9] were then generated. Figure 5.8 compares the MIXED COMPANY data to the predicted depth losses given by Equation (7.1). Generally good agreement is observed although the predictions lie on the low side of the data scatter. The same technique is then used in Section 7 to estimate fluid loss from large scale containers exposed to nuclear environments. Our findings and conclusions are presented in Subsection 6.2.

7.4 Recommendations

Technical areas where further work is necessary for a complete description of blast and shock induced fluid motion include:

- a) compressible fluid effects
- b) pressure coupling between air and fluid

- c) shear interaction between air and fluid
- d) effect of debris impact

DNA is currently studying the effect of fluid compressibility. Preliminary indications are that compressibility plays an insignificant role in the late-time fluid motion and that, consequently, the results described above will not be significantly affected. No such tentative conclusion can be made, however, for the remaining effects listed above.

REFERENCES

1. H. L. Brode, H. F. Cooper, and G. G. Leigh, "Hardness, Mobility, Dispersion, Redundancy and Mission Effectiveness Under Nuclear Attack," Presented at the Ninth Defense Research Group Seminar on Systems Concept for Hardening of Military Installations, Bodo, Norway, 14-16 September 1971. Also, Air Force Weapons Laboratory Technical Report AFWL-TR-72-18, May 1972.
2. J. J. Stoker, Water Waves, (Interscience, New York 1957), pp 9-18.
3. H. L. Brode, Annual Review of Nuclear Sciences, Vol. 18, No. 153, 1968.
4. F. R. Gilmore, Scaling the Effects of Overpressure on Bodies of Water, R & D Associates, RDA-TR-202-DNA, May 1973.
5. H. W. Liepmann and A. Roshko, Elements of Gasdynamics, (John Wiley & Sons, New York, 1957) pp 208-215.
6. S. Glasstone, The Effects of Nuclear Weapons, (SAEC, Washington D.C., 1962), pp 177-195.
7. J. W. Miles, Journal of Fluid Mechanics, Vol. 6, No. 583, 1959.
8. Personal communication between P. Liebermann, TRW Systems Group, and E. J. Chapyak, R & D Associates, October 1973.
9. E. J. Chapyak and H. F. Cooper, Jr., "Fluid Slosh Experiments" Middle North Series, MIXED COMPANY Event, Project Officer's Report 6745, Contract No. DNA001-71-C-0103, 25 July 1973.
10. D. Marsh, "Test Report for Small Pan Fluid Slosh Investigation", Wyle Laboratories Test Report 26270, December 1973.
11. G. D. Teel, "Airblast Measurements", Proceedings of the MIXED COMPANY/ MIDDLE GUST Results Meeting, Vol. 1, GE-TEMPO, DASIAC, Santa Barbara, California, pp 111-124, May 1, 1973.
12. H. F. Cooper, "Empirical Studies of Ground Shock and Strong Motions in Rock," R & D Associates, DNA 3245F, October 1973.

LIST OF SYMBOLS

- a - peak displacement amplitude of horizontal ground motion
- A_n - modal coefficients for velocity potential
- B_n - modal coefficients for surface displacement
- C_d - drag coefficient
- d - undisturbed fluid depth
- D - horizontal ground motion displacement
- \vec{D} - vector ground motion displacement
- \vec{D}^* - \vec{D}/ℓ
- D^+ - positive phase duration
- f - temporal frequency
- F_k - frequency structure function for maximum wave height
- g - gravitational constant
- h - maximum first mode wave height
- H - vertical ground motion displacement
- i - unit vector in x-direction
- I - positive phase overpressure impulse
- k - surface disturbance wave number
- \vec{k} - unit vector in z direction
- ℓ - container length
- M - mach number of airflow
- n - mode number
- P - airblast overpressure
- P^* - $P/\rho g \ell$
- Q_s - airblast dynamic pressure
- R - radius from ground zero
- t - time
- T - slosh period
- T_t - ℓ/u
- T_n - $2\pi/\omega_n$
- u - air shock propagation velocity
- V - crater volume

LIST OF SYMBOLS (continued)

W	- explosive yield
x	- horizontal dimension
z	- vertical dimension
x^*	- x/ℓ
z^*	- z/ℓ
α_n	- modal coefficients for ground displacement
β_n	- modal coefficients for airblast overpressure
δP	- overpressure perturbation induced by free surface disturbance.
Δd	- fluid depth loss
ω_n	- radian frequency of n^{th} mode
θ	- time decay constant for dynamic pressure
ϕ	- fluid velocity potential
ϕ^*	- $\phi/\sqrt{\ell^3 g}$
ψ	- reduced velocity potential
ρ	- fluid density
Γ	- constant of proportionality between wave height and depth loss
τ	- $t/\sqrt{\ell/g}$
$\vec{\nabla}$	- gradient operator
$\vec{\nabla}_*$	- $\ell \vec{\nabla}$
η	- free surface displacement
η^*	- η/ℓ

DISTRIBUTION LIST

DEPARTMENT OF DEFENSE

Assistant Secretary of Defense
Intelligence
ATTN: ODASD IA

Assistant to the Secretary of Defense
Atomic Energy
ATTN: Honorable Donald R. Cotter

Director
Defense Advanced Research Projects Agency
ATTN: STO, Kent Krosa
ATTN: NMRO
ATTN: PMO
ATTN: STO
ATTN: Tech. Lib.
ATTN: R. Chapman
ATTN: A. Tachmindji

Director
Defense Civil Preparedness Agency
ATTN: Staff Dir., Research, George N. Sisson
10 cy ATTN: Tech. Lib.

Director
Defense Communications Agency
ATTN: Code 930
ATTN: Code 930, Franklin D. Moore

Defense Documentation Center
12 cy ATTN: TC

Director
Defense Intelligence Agency
ATTN: DI-7E
ATTN: DI-7D, Edward O' Farrell
ATTN: DT-1C, Jack Vorona
ATTN: DT-2, Wpns. & Sys. Div.
ATTN: Tech. Lib.

Director
Defense Nuclear Agency
ATTN: DDST
ATTN: STSI, Archives
2 cy ATTN: SPSS
2 cy ATTN: STTL, Tech. Lib.

Chairman
Dept. of Defense Explo. Safety Board
ATTN: DD/S&SS
ATTN: Thomas Zaker

Director of Defense Research & Engineering
Department of Defense
ATTN: AD/NP
ATTN: AD/SW
ATTN: DD/S&SS
ATTN: DD/S&SS
ATTN: DD/TWP

Commander
Field Command
Defense Nuclear Agency
ATTN: FCT
ATTN: FCPR

DEPARTMENT OF DEFENSE (Continued)

Commandant
Industrial College of the Armed Forces
ATTN: Tech. Lib.

Director
Interservice Nuclear Weapons School
ATTN: Tech. Lib.

Director
Joint Strategic Target Planning Staff, JCS
ATTN: DOXT
ATTN: JLTW-2
ATTN: STINFO Library
ATTN: XPFS

Chief
Livermore Division, Field Command, DNA
ATTN: FCPRL

Commandant
National War College
ATTN: NWCLEB-CR

Weapons Systems Evaluation Group
ATTN: Doc. Con.

DEPARTMENT OF THE ARMY

Assistant Chief of Staff for Ops. & Plans
Department of the Army
ATTN: Dir. of Chem. & Nuc. Ops.
ATTN: Tech. Lib.

Commander
Ballistic Defense System Command
ATTN: BDMSC-TEN, Noah J. Hurst

Director
Ballistic Missile Defense Advanced Technical Center
Huntsville Office
ATTN: CRDABH-S
ATTN: 1CRDABH-X

Manager
Ballistic Missile Defense Program Office
ATTN: John Shea

Chief of Research, Development & Acquisition
Department of the Army
ATTN: DAMA-CSM-N, LTC E. V. DeBoeser, Jr.
ATTN: Tech. Lib.

Commander
Harry Diamond Laboratories
ATTN: AMXDO-NP
ATTN: AMXDO-RBI, John A. Rosado
ATTN: AMXDO-TI, Tech. Lib.

Department of the Army
Office Chief of Engineers
ATTN: DAEN-MCE-D
ATTN: DAEN-RDM

DEPARTMENT OF THE ARMY (Continued)

Commander
Picatinny Arsenal
ATTN: Tech. Lib.

Director
U.S. Army Ballistic Research Laboratories
ATTN: AMXBR-X, Julius J. Meszaros
ATTN: J. H. Keefer
ATTN: W. Taylor
ATTN: Tech. Lib., Edward Balcy

Commander
U.S. Army Communications Command
ATTN: Tech. Lib.

Commander
U.S. Army Electronics Command
ATTN: AMSEL-TL-IR, Edwin T. Hunter

Commander
U.S. Army Engineer Center
ATTN: ATSEN-SY-L

Project Engineer
U.S. Army Engineer District, Huntsville
ATTN: HNDSE-R, Michael M. Dembo

Division Engineer
U.S. Army Engineer District, Ohio River
ATTN: Tech. Lib.

Director
U.S. Army Engineer Waterways Experiment Station
ATTN: John N. Strange
ATTN: Guy Jackson
ATTN: Leo Ingram
ATTN: William Flathau
ATTN: Tech. Lib.

Commander
U.S. Army Mat. & Mechanics Research Center
ATTN: Richard Shea
ATTN: John Mescall
ATTN: Tech. Lib.

Commander
U.S. Army Materiel Command
ATTN: AMCRD-WN-RE, John F. Corrigan
ATTN: W. H. Hubbard
2 cy ATTN: AMCRD-BN
2 cy ATTN: AMCRD-WN
ATTN: Tech. Lib.

Commander
U.S. Army Materiel Command
ATTN: Research & Concepts Branch

Commander
U.S. Army Missile Command
ATTN: AMSMI-XS, Chief Scientist
ATTN: Tech. Lib.

Commander
U.S. Army Mobility Equipment R & D Center
ATTN: Tech. Lib.

Commander
U.S. Army Nuclear Agency
ATTN: ATCA-NAW
ATTN: Tech. Lib.

DEPARTMENT OF THE ARMY (Continued)

Commandant
U.S. Army War College
ATTN: Library

Commander
U.S. Army Weapons Command
ATTN: Tech. Lib.

DEPARTMENT OF THE NAVY

Chief of Naval Material
Navy Department
ATTN: MAT 0323

Chief of Naval Operations
Navy Department
ATTN: OP-03EG
ATTN: OP-985F

Chief of Naval Research
Navy Department
ATTN: Code 464, Jacob L. Warner
ATTN: Code 464, Thomas P. Quinn
ATTN: Tech. Lib.
2 cy ATTN: Nicholas Perrone

Officer-in-Charge
Civil Engineering Laboratory
ATTN: R. J. Odello
ATTN: Stan Takahashi
ATTN: Tech. Lib.

Commander
Naval Electronic Systems Command
Naval Electronic Systems Command Headquarters
ATTN: PME 117-21A

Commander
Naval Facilities Engineering Command
Headquarters
ATTN: Code 03A
ATTN: Code 04B
ATTN: Code 04B, M. Yachnis
ATTN: Tech. Lib.

Superintendent
Naval Postgraduate School
ATTN: Code 2124, Tech. Rpts. Librarian

Director
Naval Research Laboratory
ATTN: Code 8442, Hanson Huang
ATTN: Code 8403A, George J. O' Hara
ATTN: Code 840, J. B. Gregory
ATTN: Code 2027, Tech. Lib.
ATTN: Code 8403, Robert O. Belshem
ATTN: Code 8440, F. Rosenthal

Commander
Naval Sea Systems Command
Navy Department
ATTN: Code 03511
ATTN: Code 03511, Carl H. Pohler
ATTN: ORD-91313, Library

DEPARTMENT OF THE NAVY (Continued)

Commander

Naval Ship Engineering Center

ATTN: NSEC 6120D
ATTN: NSEC 6110.01
ATTN: NSEC 6105
ATTN: NSEC 6105G
ATTN: 6105C1
ATTN: Tech. Lib.

Commander

Naval Ship Research & Development Center

ATTN: Code 1731C
ATTN: Code 11
ATTN: Code 174, R. D. Short
ATTN: Code 1171
ATTN: Code 2740, Y. F. Wang
ATTN: Code L42-3, Library
ATTN: Code 1962
ATTN: Code 1903
ATTN: Code 19

Commander

Naval Ship Research & Development Center

ATTN: Edward W. Palmer
ATTN: John Gordon
ATTN: Code 17, William W. Murray
ATTN: Tech. Lib.

Commander

Naval Surface Weapons Center

ATTN: Code 730, Tech. Lib.
ATTN: Code 241, J. Petes
ATTN: Code 240, C. J. Aronson
ATTN: Code 243, G. Young
ATTN: Code 1224, Navy Nuc. Prgms. Off.
ATTN: Code 240, H. A. Snay

Commander

Naval Surface Weapons Center

ATTN: Tech. Lib.

Commander

Naval Undersea Center

ATTN: E. P. Cooper
ATTN: Tech. Lib.

President

Naval War College

ATTN: Tech. Lib.

Commander

Naval Weapons Center

ATTN: Carl Austin
ATTN: Paul Cordle
ATTN: Code 533, Tech. Lib.

Commanding Officer

Naval Weapons Evaluation Facility

ATTN: R. Hughes
ATTN: Tech. Lib.

Director

Strategic Systems Project Office

ATTN: NSP-272
ATTN: NSP-273
ATTN: NSP-43, Tech. Lib.

DEPARTMENT OF THE AIR FORCE

Commander

ADC/DE

ATTN: DDEEN

Commander

ADC/XP

ATTN: XP
ATTN: XPQDQ

Commander

Aeronautical Systems Division, AFSC

ATTN: Tech. Lib.

AF Armament Laboratory, AFSC

ATTN: DLOSL, Library

AF Cambridge Research Laboratories, AFSC

ATTN: LWW, Ker C. Thompson
ATTN: SUOL, AFCL Research Library

AF Institute of Technology, AU

ATTN: Library, AFIT, Bldg. 640, Area B

AF Weapons Laboratory, AFSC

ATTN: DE-I
ATTN: DEV, Jimmie L. Bratton
ATTN: DEV, M. A. Plamondon
ATTN: DEX
ATTN: Robert Henny
ATTN: Robert Port
ATTN: SUL

Headquarters

Air Force Systems Command

ATTN: DLCAW
ATTN: Tech. Lib.

Commander

Armament Development & Test Center

ATTN: ADBRL-2
ATTN: Tech. Lib.

Commander

Foreign Technology Division, AFSC

ATTN: ETET, Capt Richard C. Husemann
ATTN: TDFBD
ATTN: TDFMG
ATTN: TD-BTA, Library

HQUSAF/IN

ATTN: IN
ATTN: INATA

HQUSAF/PR

ATTN: PRE

HQUSAF/RD

ATTN: RDQPN
ATTN: RDPM

Commander

Rome Air Development Center, AFSC

ATTN: EMREC, R. W. Mair
ATTN: EMTLD, Doc. Lib.

SAMSO/DE

ATTN: DEB

DEPARTMENT OF THE AIR FORCE (Continued)

SAMSO/DY
ATTN: DYS

SAMSO/MN
ATTN: MNN
ATTN: MMH
ATTN: MNI
ATTN: MNNH

SAMSO/XR
ATTN: XRTB

Commander in Chief
Strategic Air Command
ATTN: NRI-STINFO Library
ATTN: XPFS

ENERGY RESEARCH & DEVELOPMENT ADMINISTRATION

Division of Military Application
U.S. Energy Research & Development Administration
ATTN: Doc. Con. for Test Office

Holmes & Narver, Inc.
ATTN: R. Kennedy

University of California
Lawrence Livermore Laboratory
ATTN: Robert Schock
ATTN: Ted Butkovich
ATTN: D. M. Norris, L-90
ATTN: Richard G. Dong, L-424
ATTN: Jack Kahn
ATTN: J. Coruthers, L-18
ATTN: Douglas Stephens
ATTN: J. R. Hearst, L-41
ATTN: Larry W. Woodruff, L-125
ATTN: Tech. Info. Dept., L-3

Los Alamos Scientific Laboratory
ATTN: Doc. Con. for Reports Library
ATTN: Doc. Con. for G. R. Spillman
ATTN: Doc. Con. for Al Davis

Sandia Laboratories
Livermore Laboratory
ATTN: Doc. Con. for L. Hill
ATTN: Doc. Con. for Tech. Lib.

Sandia Laboratories
ATTN: Doc. Con. for M. L. Merritt
ATTN: Doc. Con. for W. Roherty
ATTN: Doc. Con. for 3141, Sandia Rpt. Coll.
ATTN: Doc. Con. for A. J. Chaban
ATTN: Doc. Con. for Luke J. Vortman

U.S. Energy Research & Development Administration
Albuquerque Operations Office
ATTN: Doc. Con. for Tech. Lib.

U.S. Energy Research & Development Administration
Division of Headquarters Services
ATTN: Doc. Con. for Class. Tech. Lib.

U.S. Energy Research & Development Administration
Nevada Operations Office
ATTN: Doc. Con. for Tech. Lib.

ENERGY RESEARCH & DEVELOPMENT ADMINISTRATION
(Continued)

Union Carbide Corporation
Hollifield National Laboratory
ATTN: Civil Def. Res. Proj.
ATTN: Doc. Con. for Tech. Lib.

OTHER GOVERNMENT AGENCIES

Bureau of Mines
Twin Cities Research Center
ATTN: Tech. Lib.

Central Intelligence Agency
ATTN: RD/SI for NED/OSI-5G48 Hqs.

Department of the Interior
Bureau of Mines
ATTN: Tech. Lib.

Department of the Interior
Bureau of Mines
ATTN: James J. Scott

Department of the Interior
U.S. Geological Survey
ATTN: J. H. Healy
ATTN: Cecil B. Raleigh

DEPARTMENT OF DEFENSE CONTRACTORS

Aerospace Corporation
ATTN: Prem N. Mathur
ATTN: Tech. Info. Services

Agabian Associates
ATTN: M. Agabian

Analytic Services, Inc.
ATTN: George Hesselbacher

Applied Theory, Inc.
2 cy ATTN: John G. Trullo

Artec Associates, Inc.
ATTN: Steven Gill

Avco Research & Systems Group
ATTN: Research Library, A-830, Rm. 7201

Battelle Memorial Institute
ATTN: R. W. Klingsmith
ATTN: Tech. Lib.

The BDM Corporation
ATTN: A. Lavagnino
ATTN: Tech. Lib.

The BDM Corporation
ATTN: Richard Hensley

The Boeing Company
ATTN: Aerospace Library
ATTN: R. H. Carlson

Brown Engineering Company, Inc.
ATTN: Manu Patel
ATTN: J. Cahoon

DEPARTMENT OF DEFENSE CONTRACTORS (Continued)

California Institute of Technology
ATTN: Thomas J. Ahrens

California Research & Technology, Inc.
ATTN: Ken Kreyenhagen
ATTN: Tech. Lib.

University of California
ATTN: G. Sackman

Calspan Corporation
ATTN: Tech. Lib.

Cambridge Acoustical Assoc., Inc.
ATTN: M. C. Junger

Civil/Nuclear Systems Corporation
ATTN: T. A. Duffy
ATTN: Robert Crawford

Columbia University
Dept. of Civil Engineering
ATTN: H. Blatch
ATTN: F. DiMaggio

University of Dayton
ATTN: Hallock F. Swift

University of Denver
Colorado Seminary
ATTN: Sec. Officer for J. Wisotski
ATTN: Sec. Officer for Tech. Lib.

EG&G, Inc.
Albuquerque Division
ATTN: Tech. Lib.

Environmental Research Corporation
ATTN: W. W. Hays

General American Transportation Corporation
General American Research Division
ATTN: G. L. Neidhardt

General Dynamics Corporation
Electric Boat Division
ATTN: L. H. Chan

General Electric Company
Space Division
ATTN: M. H. Bortner, Space Sci. Lab.

General Electric Company
Re-Entry & Environmental Systems Division
ATTN: Arthur L. Ross

General Electric Company
TEMPO-Center for Advanced Studies
ATTN: DASIAC

General Research Corporation
ATTN: Benjamin Alexander

IIT Research Institute
ATTN: R. E. Welch
ATTN: Milton R. Johnson
ATTN: Tech. Lib.

DEPARTMENT OF DEFENSE CONTRACTORS (Continued)

Institute for Defense Analyses
ATTN: IDA, Librarian, Ruth S. Smith

J. H. Wiggins, Co. Inc.
ATTN: John Collins

J. L. Merritt
Consulting & Special Engr. Svs., Inc.
ATTN: J. L. Merritt
ATTN: Tech. Lib.

Kaman Avidyne
Division of Kaman Sciences Corporation
ATTN: Norman P. Hobbs
ATTN: E. S. Criscione
ATTN: G. Zartarian
ATTN: Tech. Lib.

Kaman Sciences Corporation
ATTN: Paul A. Ellis
ATTN: Frank H. Shelton
ATTN: Library

Lockheed Missiles & Space Co. Inc.
ATTN: Tech. Lib.

Lockheed Missiles & Space Company
ATTN: Tom Geers, Dept. 52-33, Bldg. 205
ATTN: Tech. Info. Ctr., D/Coll.

Lovelace Foundation for Medical Education
ATTN: Asst. Dir. of Res., Robert K. Jones
ATTN: Tech. Lib.

Martin Marietta Aerospace
Orlando Division
ATTN: G. Fotteo

University of Maryland
Dept. of Civil Engineering
ATTN: Bruce S. Berger

McDonnell Douglas Corporation
ATTN: Robert W. Halprin

Meteorology Research, Inc.
ATTN: William D. Green

The Mitre Corporation
ATTN: Library

Nathan M. Newmark
Consulting Engineering Services
ATTN: Nathan M. Newmark

Pacifica Technology
ATTN: J. Kent
ATTN: R. Bjork

Physics International Company
ATTN: Doc. Con. for Dennis Orphal
ATTN: Doc. Con. for E. T. Moore
ATTN: Doc. Con. for Larry A. Behrmann
ATTN: Doc. Con. for Tech. Lib.
ATTN: Doc. Con. for Coye Vincent
ATTN: Doc. Con. for Fred M. Sauer
ATTN: Doc. Con. for Robert Swift
ATTN: Doc. Con. for Charles Godfrey

DEPARTMENT OF DEFENSE CONTRACTORS (Continued)

Polytechnic Inst. of Brooklyn
Dept. of Aerospace & Applied Mech.
ATTN: J. M. Klosner

R & D Associates
ATTN: William B. Wright, Jr.
ATTN: Sheldon Schuster
ATTN: Tech. Lib.
ATTN: Albert L. Latter
ATTN: Cyrus P. Knowles
ATTN: Bruce Hartenbaum
ATTN: J. G. Lewis
ATTN: Henry Cooper
ATTN: Harold L. Brode
ATTN: Jerry Carpenter
ATTN: E. J. Chapyak

The Rand Corporation
ATTN: C. C. Mow

Research Analysis Corporation
ATTN: Documents Library

Science Applications, Inc.
ATTN: D. E. Maxwell
ATTN: David Bernstein

Science Applications, Inc.
ATTN: William M. Layson
ATTN: R. Seebaugh
ATTN: John Mansfield

Science Applications, Inc.
ATTN: Michael McKay
ATTN: Tech. Lib.

Science Applications, Inc.
ATTN: R. A. Shunk

Shock Hydrodynamics, Inc.
A Div. of Whittaker Corporation
ATTN: L. Zernow

Southwest Research Institute
ATTN: Wilfred E. Baker
ATTN: A. B. Wenzel

Stanford Research Institute
ATTN: SRI Library, Rm. G-021
ATTN: Carl Peterson
ATTN: Burt R. Gasten
ATTN: George R. Abrahamson

Sundstrand Corporation
ATTN: Curtis B. White

DEPARTMENT OF DEFENSE CONTRACTORS (Continued)

Systems, Science & Software, Inc.
ATTN: Ted Cherry
ATTN: Robert T. Allen
ATTN: Thomas D. Riney
ATTN: Donald R. Grine
ATTN: Tech. Lib.

Terra Tek, Inc.
ATTN: A. H. Jones
ATTN: Sidney Green
ATTN: Tech. Lib.

Tetra Tech, Inc.
ATTN: Li-San Hwang
ATTN: Tech. Lib.

TRW Systems Group
ATTN: Benjamin Sussholtz
ATTN: Norm Lipner
ATTN: William Rowan
ATTN: Jack Farrell
ATTN: Tech. Info. Ctr., S-1930
ATTN: Pravin Bhutta
ATTN: Paul Lieberman

TRW Systems Group
San Bernardino Operations
ATTN: Greg Hulcher

Universal Analytics, Inc.
ATTN: E. I. Field

URS Research Company
ATTN: Ruth Schneider
ATTN: Tech. Lib.

The Eric H. Wang
Civil Engineering Research Facility
ATTN: Larry Bickle
ATTN: Neal Baum

Washington State University
Administrative Office
ATTN: Arthur Miles Hohorf for George Duval

Weidlinger Assoc. Consulting Engineers
ATTN: Melvin L. Baron

Weidlinger Assoc. Consulting Engineers
ATTN: J. Isenberg

Westinghouse Electric Company
Marine Division
ATTN: W. A. Volz